Ore Geology Reviews 189 (2026) 107117

Contents lists available at ScienceDirect

Ore Geology Reviews

journal homepage: www.elsevier.com/locate/oregeorev

# Hydrothermal germanium mineralization at South Lakes Glacier in the Black Angel Zn-Pb district, West Greenland

Michael Eigler [a,b,*], Benjamin F. Walter [c], R. Johannes Giebel [d,e], Jochen Kolb [a,b]

[a] Chair of Geochemistry and Economic Geology, Institute of Applied Geosciences (AGW), Karlsruhe Institute of Technology (KIT), Adenauerring 20b, 76131 Karlsruhe, Germany
[b] Laboratory of Environmental and Raw Material Analysis (LERA), AGW, KIT, Adenauerring 20b, 76131 Karlsruhe, Germany
[c] Petrology and Mineral Resources, Department of Geosciences, University of Tübingen, Schnarrenbergstrasse 92-94, 72074 Tübingen, Germany
[d] Institute of Applied Geosciences, Technische Universität Berlin, Ernst-Reuter-Platz 1, 10587 Berlin, Germany
[e] Department of Geology, University of the Free State, 250 Nelson-Mandela-Drive, Bloemfontein 9300, South Africa

ARTICLE INFO

*Keywords:*
Briartite
Zn-Pb deposit
Remobilization
Critical metals
Syn-metamorphic
Rinkian

ABSTRACT

Metamorphosed Zn-Pb deposits can host significant amounts of critical metals, but their enrichment and source are often not well understood. The Black Angel district in central West Greenland hosts several marble-hosted Paleoproterozoic Zn-Pb occurrences, including the Black Angel mine. The sphalerite-pyrite-galena dominated massive sulfides in the district host briartite, a rare Cu-thiogermanate mineral. Detailed petrographic studies, electron microprobe and laser ablation-inductively coupled plasma-mass spectrometry and micro-XRF-mapping were applied to breccia-hosted massive sulfide from the South Lakes Glacier prospect in the Black Angel district to study the formation of briartite and the distribution of Ge in the ore. Whole rock analyses reveal Ge grades of 120 ppm in the ore. Briartite, occurring as clusters of μm-sized grains, as well as anhedral grains of up to three millimeters in diameter, formed by precipitation from Cu-Ge-bearing hydrothermal fluids coevally with Ge-rich chalcopyrite and is the main host for Ge. Unusually Ge-rich phengite and quartz post-dating briartite reflect a shift in Ge behaviour from sulfide-hosted to silicate-hosted. The epigenetic ore assemblage was overprinted by metamorphism leading to solid-state and dissolution-precipitation sulfide remobilization as well as the formation of a *syn*-metamorphic ore stage. Remobilization led to widespread sulfide breccia formation at South Lakes Glacier. Biotite and graphite geothermometry reveal peak metamorphic temperatures of ~500°C.

## 1. Introduction

Germanium (Ge) is a metalloid listed as critical raw material by the European Union and the United States of America (European Commission, 2020; U.S. Geological Survey, 2024). It is widely used for high-tech applications such as fiber optic cables, infrared optics, solar applications and polymerization catalysts. Germanium is a frequently unreported and overlooked trace element which contributes to a lack of reliable bulk geochemical data, even within larger ore deposits (Höll et al., 2007). Germanium has an average crustal abundance of 1.5 ppm, is mainly produced as a by-product from coal fly ash and Zn-Pb mining. It is concentrated in carbonate-hosted Mississippi Valley-type (MVT) and Kipushi-type (KPT) deposits, as well as clastic-dominated Zn-Pb deposits (Paradis, 2015; Shanks et al., 2017; Torró et al., 2023). Germanium commonly occurs as traces in various deposit types but is rarely highly concentrated, though it may occur in discrete, highly Ge-enriched phases in some deposit types, mainly in KPT deposits, but also volcanogenic massive sulfide and epithermal deposits (Intiomale and Oosterbosch, 1974; Kampunzu et al., 2009; Melcher, 2003; Paar and Putz, 2005; Vikentyev et al., 2016; Wagner and Monecke, 2005). In undeformed MVT deposits and vein-type Zn-Pb deposits, Ge is dominantly hosted in the sphalerite crystal lattice (Belissont et al., 2014; Torró et al., 2023). Germanium contents may reach up to 3000 ppm Ge in various sphalerite types, from acicular to euhedral undeformed crystals (Belissont et al., 2014; Bernstein, 1985; Luo et al., 2022). Several substitution mechanisms have been proposed to explain Ge incorporation in sphalerite, e.g. direct substitution of $Ge^{4+}$ for $Zn^{2+}$ or coupled substitution with monovalent cations such as $Cu^{+}$ and $Ag^{+}$ or divalent cations

* Corresponding author at: Chair of Geochemistry and Economic Geology, Institute of Applied Geosciences (AGW), Karlsruhe Institute of Technology (KIT), Adenauerring 20b, 76131 Karlsruhe, Germany.
*E-mail address:* michael.eigler@kit.edu (M. Eigler).

https://doi.org/10.1016/j.oregeorev.2026.107117
Received 14 July 2025; Received in revised form 14 November 2025; Accepted 15 January 2026
Available online 17 January 2026

like $Pb^{2+}$ and $Mn^{2+}$ (Belissont et al., 2014; Belissont et al., 2016; Cugerone et al., 2021; Liu et al., 2023; Luo et al., 2022). In KPT and epithermal deposits, Ge is mainly hosted by (Cu-)thiogermanates, such as briartite [$Cu_2(Fe,Zn)GeS_4$], renierite [$(Cu,Zn)_{11}(Ge,As)_2Fe_4S_{16}$], germanite [$Cu_{13}Fe_2Ge_2S_{16}$], germanocolusite [$Cu_{13}V(As,Ge)_3S_{16}$] and argyrodite [$Ag_8GeS_6$] (De Vos et al., 1974; Geier and Otteman, 1970; Intiomale and Oosterbosch, 1974; Melcher, 2003; Melcher et al., 2006; Paar and Putz, 2005) which are thought to form from Ge-bearing hydrothermal fluids with a high sulfidation state (Bernstein, 1985; Kampunzu et al., 2009; Melcher, 2003). In metamorphosed Zn-Pb deposits recrystallisation and remobilization can have a significant impact on the distribution of critical and trace elements, including Ge (Cugerone et al., 2020; Fougerouse et al., 2023; Tiu et al., 2021). The occurrence of accessory Ge-phases (e.g. briartite) in deposits of the Pyrenean Axial Zone has been linked to dynamic recrystallisation of sphalerite (Cugerone et al., 2018).

Recently, briartite was reported from the former Black Angel mine, where it is found in association with sphalerite (Horn et al., 2019). The Black Angel mine in central West Greenland, active from 1973 to 1990, produced 11.2 Mt with 12.3 % Zn, 4.1 % Pb and 29 ppm Ag from ten marble-hosted ore bodies (Thomassen, 2003). While major base and precious metals contents were reported during production times (van der Stijl, 1990), the critical element distribution was never evaluated. New whole rock data of massive sulfide ore from the South Lakes Glacier occurrence in the Black Angel district show mean Ge grades of 120 ppm and mean Ga grades of 130 ppm (Supplementary Table 1), indicating a significant, previously unrecognized Ge and Ga endowment, and making Black Angel an ideal place to study the formation of Ge-bearing Zn-Pb deposits. The formation of discrete Ge phases is not well understood, but knowledge of these processes is vital for future exploration and exploitation efforts. Like many other Zn-Pb or polymetallic districts (e.g. Broken Hill, Red Dog or Mt. Isa) the Black Angel district has been subject to deformation and metamorphism (Horn et al., 2019; Partin et al., 2021; Pedersen, 1980; Pedersen, 1981). Formation of briartite in the Black Angel district may therefore either be related to metamorphic recrystallisation and remobilization, as in the Pyrenean deposits, or may have formed by direct precipitation from Ge-bearing hydrothermal fluids. While the Black Angel mine itself is now inaccessible, the South Lakes Glacier occurrence within the district offers the chance to characterize the deformation processes affecting the ore and mechanisms of briartite formation.

Metamorphic conditions at Black Angel are not well constrained but are vital for understanding potential processes affecting the ore. This study aims at better constraining: (1) formation of discrete Ge minerals

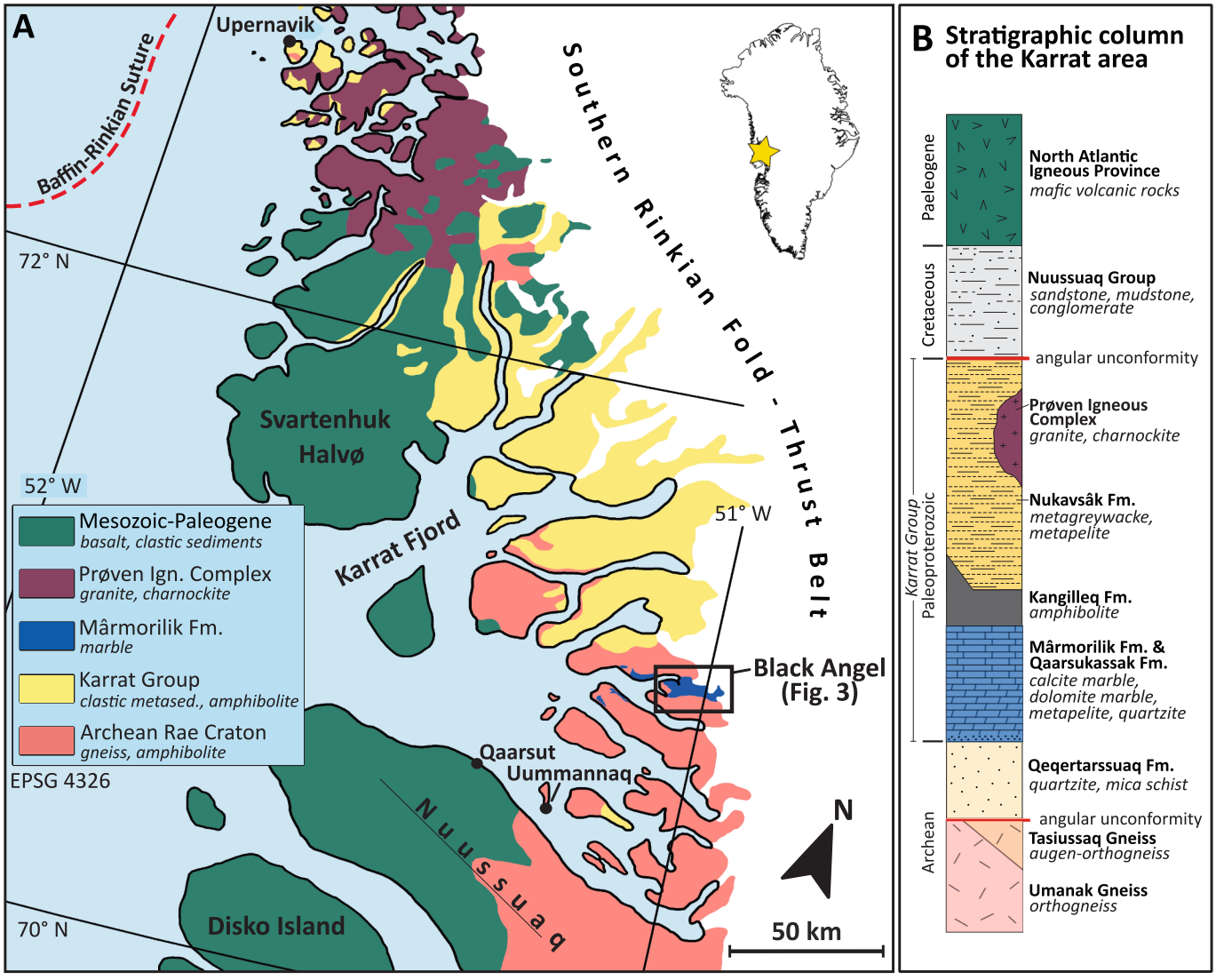


**Fig. 1.** A) Simplified overview of the southern Rinkian Orogen of central West Greenland (modified after Grocott et al., 2023). B) Stratigraphic column of the Karrat Fjord area (after Grocott and McCaffrey, 2017; Grocott et al., 2023).

in Zn-Pb deposits; (2) genesis of mineralization at South Lakes Glacier and in the Black Angel district; and (3) the metamorphic temperature conditions in the Black Angel district by investigating petrography and mineral chemistry of sulfides and micas using electron microprobe analysis (EMPA), laser ablation inductively coupled plasma mass spectrometry (LA-ICP-MS) and micro-XRF mapping. Multiple geothermometers were applied to determine metamorphic temperature conditions At South Lakes Glacier.

## 2. Geological setting

### 2.1. The Karrat Group and Rinkian Orogen

The Black Angel district is located between Nuussuaq peninsula and the Karrat Fjord of central West Greenland (Fig. 1A). It is dominated by Paleoproterozoic metasedimentary and metavolcanic rocks of the Karrat Group, which unconformably overlie the Archean Rae craton (Guarnieri et al., 2022; Henderson and Pulvertaft, 1987). The Karrat Group was deposited between ca. 2000 Ma and 1850 Ma (Guarnieri et al., 2023). The lower Karrat Group consists of marble and clastic metasedimentary rocks of the Mârmorilik Formation and the laterally equivalent Qaarsukassak Formation (Fig. 1B; Guarnieri and Baker, 2022; Guarnieri et al., 2022). This is overlain by metagraywacke and metapelite of the Nûkavsak Formation and intercalated amphibolite of the Kangilleq Formation (Fig. 1B; Grocott and McCaffrey, 2017; Henderson and Pulvertaft, 1987; Partin et al., 2024). The Black Angel district is part of the Rinkian Orogen, an Andean-type orogen linking western Greenland and Baffin Island which is considered part of the Trans-Hudson Orogen (Grocott et al., 2023; Guarnieri et al., 2023). Peak metamorphism was dated at ca. 1830—1810 Ma on apatite and detrital zircon (Kirkland et al., 2017; Thrane, 2021). Sidgren et al. (2006) report $^{40}$Ar-$^{39}$Ar cooling ages ranging from 1795 ± 3 to 1782 ± 3 Ma for hornblende from Archean rocks of the southern Rinkian Orogen. Kirkland et al. (2017) provide titanite U-Pb ages of 1768 ± 8 Ma reflecting metamorphic crystallization. The rocks of the Karrat Group occur in a fold-and-thrust belt thought to represent an inverted back-arc basin associated with arc-continent collision (Grocott et al., 2023; Guarnieri et al., 2023; Partin et al., 2024). The deformation history of the southern Rinkian Orogen is complex and controversial. Grocott et al. (2023) identify three regional deformation events in the southern Rinkian Orogen: (1) eastward thrusting with close to tight folding beginning at ca. 1870 Ma ($D_1$); succeeded by (2) subsequent westward, thick-skinned inversion tectonics reworking older structures ($D_2$) between 1830 and 1820 Ma; and (3) continued high-temperature deformation associated with N-S shortening by bivergent detachment folding and thrusting at ca. 1820 – 1810 Ma ($D_3$) (Fig. 2). Thus, $D_2$ and $D_3$ of Grocott et al. (2023) coincide with available ages for peak metamorphism. Guarnieri et al. (2023) report one collisional stage leading to regional Rinkian metamorphism between 1830–1800 Ma with folding and thrusting postdating the regional metamorphism (Fig. 2). However, Guarnieri and Baker (2022) describe two deformation events affecting the Black Angel area: (1) the first event is characterized by NNE-SSW oriented maximum horizontal stress and SW-ward thick-skinned thrusting ($D_1$); and (2) a second stage of brittle deformation caused the inversion of pre-existing normal faults during NW-SE compression, with SE-ward propagation, refolding and breaching of previous thrust contacts ($D_2$) (Fig. 2). This study follows the $D_1$ and $D_2$ classification of Guarnieri and Baker (2022).

### 2.2. The Black Angel district

The Zn-Pb occurrences of the Black Angel district are hosted by the Mârmorilik Formation consisting of calcitic and dolomitic marble with intercalated graphitic metapelite and chert (Fig. 3; King, 1983). The Mârmorilik Formation is divided into two tectonostratigraphic units separated and tectonically stacked by the Nunngarut thrust (Fig. 3; Guarnieri et al., 2022): (1) the South Lakes Unit forms the footwall and consists of a basal quartzite member overlain by quartz- and tremolite-bearing dolomite marble, pure dolomite marble, minor calcite marble and graphitic metapelite (King, 1983; Pedersen, 1978); and (2) the Black Angel Unit in the hanging wall contains banded and massive calcite marble, minor dolomite marble with locally preserved stromatolitic textures and intercalated graphitic metapelite. Marble commonly contains anhydrite and scapolite, interpreted as metamorphic relics of evaporites (Rosa et al., 2023), and vuggy zones in ore-bearing horizons of the Black Angel mine that potentially represent leached evaporites (Harris, 1986). In the South Lakes area, N-S to NE-SW trending *syn*-sedimentary, listric normal faults are prominent, that were reactivated and inverted during ($D_2$) (Fig. 3; Guarnieri and Baker, 2022).

The Black Angel mine consists of ten ore bodies: Angel, Cover, Tributary, V16, I, I South, Banana, Deep Ice, Nunngarut 1 and Nunngarut 2 (Fig. 3). Angel and Cover are the largest ore bodies containing around 78 % of the total ore (van der Stijl, 1990). These ore bodies are hosted by calcite marble of the Black Angel Unit (Fig. 3) and form flat-lying sheets up to 600 m wide, 1000 m long and 0.5 – 35 m thick (Pedersen, 1981). These sheets occur in the core of roughly WNW-ESE trending isoclinal folds and are subparallel to the $S_1$ foliation of the marble (Pedersen, 1980). The Angel orebody was metamorphosed and deformed during $D_1$ (Guarnieri and Baker, 2022) showing isoclinal to tight folding with E-trending fold axis, southward thrusting with thrust sheets subparallel to the ore body and N-vergent open to tight folding with fold axes trending 90-125° (Pedersen, 1980). Four ore textures are distinguished in the Angel ore body (Pedersen, 1980): (1) “banded ore”

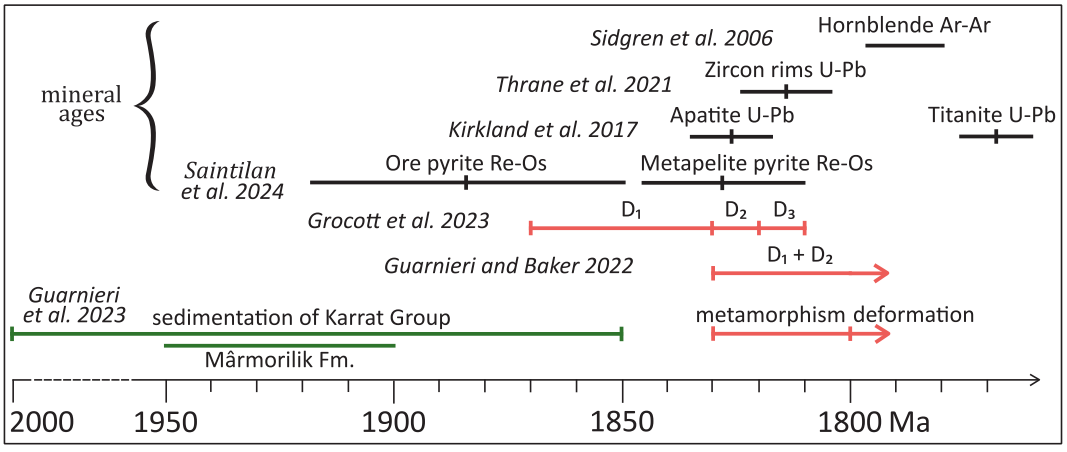


**Fig. 2.** Comparison of available age data and interpretations of deformation history of the Karrat area (Sidgren et al., 2006; Kirkland et al., 2017; Thrane, 2021; Guarnieri and Baker, 2022; Grocott et al., 2023; Guarnieri et al., 2023; Saintilan et al., 2024).

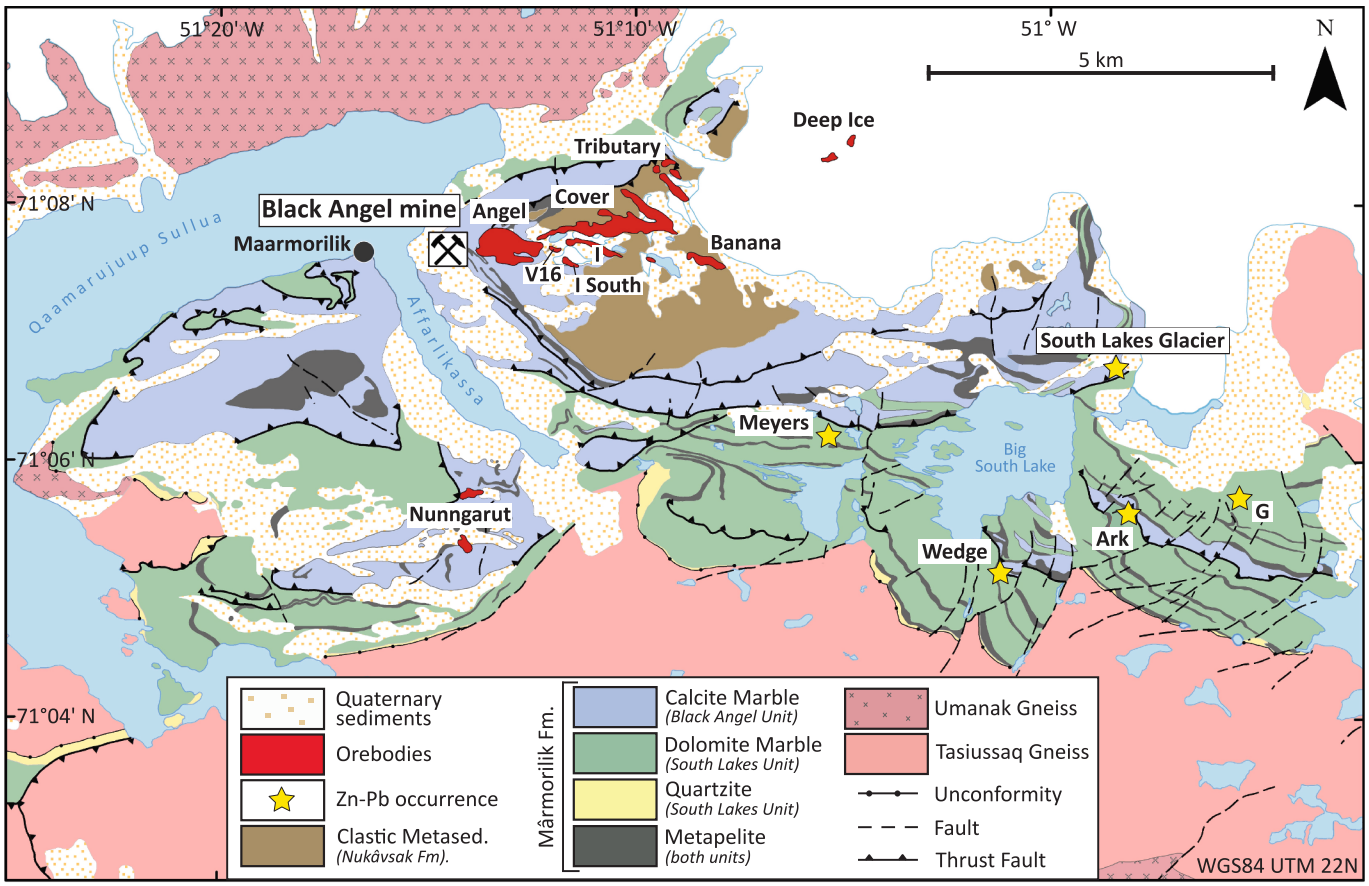


**Fig. 3.** Geological map of the Black Angel district in central West Greenland with surface projection of orebodies of the Black Angel mine and further Zn-Pb occurrences (modified after King, 1983; Thomassen, 2003; Guarnieri et al., 2022).

with alternating mm- to cm-thick bands of pyrite and sphalerite-galena interpreted as syngenetic and primary ore texture (Pedersen, 1980; Partin et al., 2021); (2) sphalerite-galena dominated "massive ore" thought to have formed from banded ore by homogenization due to deformation; (3) "porphyroclastic ore" with cm-sized, rounded pyrite in fine-grained sphalerite-galena matrix; and (4) coarse-grained "remobilized ore" in the northern part of the orebody.

The ore is dominated by sphalerite, galena and pyrite with minor amounts of chalcopyrite and other sulfides (Pedersen, 1980; Horn et al., 2019). Saintilan et al. (2024) determined a Re-Os age of 1884 ± 35 Ma for pyrite from the massive ore of the Angel ore body and a Re-Os age of 1828 ± 17 Ma for pyrite in metapelite wallrock. The deposit has been interpreted as MVT deposit based on Re-Os data, meta-carbonate host rock and the presence of meta-evaporite (Hughes, 1982; Partin et al., 2021; Rosa et al., 2023; Saintilan et al., 2024). Horn et al. (2019) interpret the Black Angel deposit as KPT deposit based on the occurrence of briartite, high fluid temperatures and *syn*-tectonic mineralization.

Outside the Black Angel mine, several sulfide occurrences hosted by both the Black Angel Unit and the South Lakes Unit have been mapped throughout the district, namely South Lakes Glacier, G, Ark, Wedge and Meyers (Fig. 3). The most prominent massive sulfide occurrence is the South Lakes Glacier prospect at the edge of the inland ice, where sulfide mineralization occurs over several hundred meters. The mineralization at South Lakes Glacier is dominated by massive sulfide breccias similar to the "porphyroclastic ore" of the Angel orebody and is hosted in folded and foliated dolomite marble (Fig. 4). The South Lakes Glacier occurrence is located in roughly NNE-SSW oriented $D_1$ fold structures and is the focus of this study.

## 3. Methodology

Nine representative hand samples of the mineralization and its host rocks were collected during field work at South Lakes Glacier. Petrography of ore and host rock was investigated with transmitted and reflected light microscopy, as well as scanning electron microscopy and cathodoluminescence on 29 polished thin sections (Supplementary Table 1).

### 3.1. Electron microprobe analysis (EMPA)

Major element composition of sulfides was determined using a JEOL JXA-8230 electron microprobe at the Petrology and Mineral Resources Group at the University of Tübingen. The analyzed elements are Zn, Pb, Ag, Cu, Fe, S, Sn, As, Sb, Mn, Cd, Te, Se, Bi and Ge (Supplementary Table 2). Analyses were conducted in wavelength-dispersive mode with an acceleration voltage of 25 kV, a probe current of 20nA and with a beam diameter of 5 μm. Counting times for major elements were 16/8 s (peak/background) and 30/15 s for minor elements. An internal overlap correction for Bi to Ge with a factor of 0.0023 was applied. Phi-Rho-Z (PRZ) correction was applied to all sulfides for data processing. Sulfide analyses with totals outside the 100 ± 2 w% range were rejected.

Major element composition of biotite and phengite was determined with the same equipment. Analyzed elements are Na, Mg, F, Si, Al, K, Cl, Ca, Ti, Ba, Fe and Mn (Supplementary Table 2). Analyses were conducted in wavelength-dispersive mode with an acceleration voltage of 15 kV, a probe current of 20nA and focused beam with a diameter of 5 μm. Counting times for major elements were 16/8 s (peak/background) and 30/15 s for minor elements. Internal overlap correction of Ba to Ti, Ti to Ba and F to Fe were applied (Supplementary Table 2). PRZ

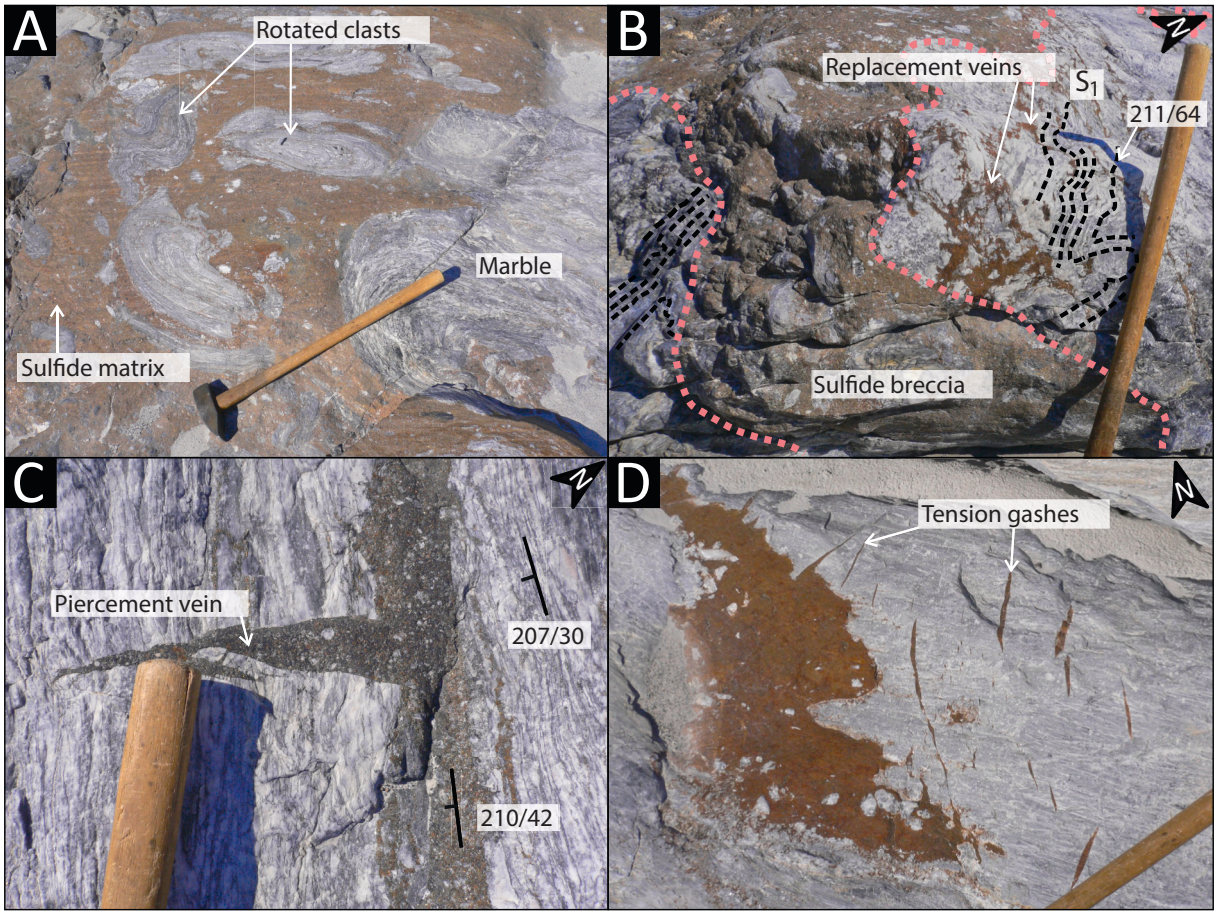


**Fig. 4.** Field photographs of sulfide mineralization at the South Lakes Glacier prospect. A) Sulfide breccia with rotated marble clasts floating in sphalerite matrix. Note isoclinal folds in the clasts. B) Sulfide breccia appearing subparallel to the regional $S_1$ foliation in the outcrop surface clearly crosscuts the foliation in this three-dimensional exposure. Orientation of $S_1$ foliation in marble is 211/64 (dip direction/dip). Arborescent propagation of brown sphalerite replacement veins cross-cutting marble. C) Thin sulfide breccia vein (210/42 dip direction/dip) subparallel to $S_1$ foliation of marble (207/30 dip direction/dip). A piercement vein crosscuts marble foliation at right angle. D) Sphalerite vein and sphalerite-filled tension gashes crosscutting foliation. Tension gashes have a N-S to NW-SE orientation.

correction was applied for data processing. Results of electron microprobe analyses are available in Supplementary Table 3.

### 3.2. Whole rock analysis

Whole rock analysis was conducted for three massive sulfide samples (Supplementary Table 1). The major element composition was determined by Optical Emission Spectroscopy (OES) and Carbon-Sulfur Analysis. The samples were digested using a microwave assisted procedure. First, 4 mL $HNO_3$ (65 %, subboiled), 2,5 mL HCl (32 %, suprapur), 1 mL HF (48 %, p.A.) were added to 100 mg of milled sample material. The mixture was heated stepwise to 220 °C and held at temperature for 30 min. Then, 5 mL of boric acid were added. During heating, the fluorides are redissolved. The final residue was dissolved in 50 mL of ultrapure water. The major element concentration in the digest was measured with a Thermo Fisher ICP-OES iCap 7000 in a radial or axial mode. All samples were prediluted to minimize interferences and assure an optimal measurement range. The certified reference materials GRX-4 (copper mill-head powder, USGS), GRX-5 (soil powder, USGS) and TUBAF (Pb-Zn-sulfide ore, house standard) were repeatedly measured to determine precision and accuracy of the measurements. Furthermore, blanks and duplicates were added to the analysis protocol. The total carbon and sulfur of the bulk rock material was determined using an Eltra CS 2000 Carbon-Sulfur Analyzer. Powdered material was heated to 2000 °C in an induction furnace with added Fe chips and W granules. Released $CO_2$ and $SO_2$ were quantified via IR spectrometry after passing through several traps to ensure dust and $H_2O$ removal. A steel standard (92400–3050; Eltra) and a barium sulfate standard (90821; Eltra) were used as reference materials to monitor analytical precision (<0.3 % for carbon, <0.6 % for sulfur).The trace element geochemistry was determined with Inductively Coupled Plasma Mass Spectrometry (ICP-MS) using a Thermo Fisher Scientific iCap RQ with helium as collision gas on the same digest. The certified reference materials CRM-TMDW-A (High-Purity standards, Inc.), TUBAF, GXR-4 and EMS-1 (metalliferous shale, GeoPT) were used for quality assurance. Argon gas flows were as follows: nebulizer gas flow 0.88 L/min, auxiliary gas flow 0.68 L/min, and cooling gas flow 13 L/min.

### 3.3. Raman spectroscopy of graphite

Raman spectra were collected with a Bruker Senterra Raman microscope at KIT, using a depolarized green laser at 532 nm wavelength and 2 mW power. Spectra were collected over a range of 70 – 2740 $cm^{-1}$ with a resolution of 3 – 5 $cm^{-1}$. Measuring time was 60 s (integration time 6 s with 10 co-additions). The samples were cut parallel to foliation. Sample polishing can have a significant effect on the crystal structure of graphite, and thus on the resulting Raman spectra (Beyssac et al., 2003). To avoid such mechanically modified grains, the laser was focused only on grains located beneath the sample surface covered by adjacent transparent minerals. The Raman spectra were evaluated using the IFORS software following the automated approach by Lünsdorf and Lünsdorf (2016) and Lünsdorf et al. (2017) minimizing user-introduced

uncertainties. 45 spot measurements on 7 graphite grains were conducted and a median temperature calculated for each grain (Supplementary Table 4).

### 3.4. Laser ablation inductively coupled mass spectrometry (LA-ICP-MS)

Trace element composition of sulfides was measured in situ by LA-ICP-MS using a Teledyne 193 nm Excimer Laser coupled to an ThermoScientific Element XR sector field ICP-MS at KIT with spot sizes ranging from 25-40 μm, laser frequency of 10 Hz, fluence of 5 J/cm$^2$, He flow of 0.3 l/min (cell), 0.2 l/min (cup) and $N_2$ flow 12 ml/min. A gas blank was analyzed for 20 s for each spot, followed by 20 s of ablation. The analyzed isotopes are $^{47}$Ti, $^{51}$V, $^{55}$Mn, $^{57}$Fe, $^{59}$Co, $^{60}$Ni, $^{63}$Cu, $^{66}$Zn, $^{69}$Ga, $^{71}$Ga, $^{72}$Ge, $^{73}$Ge, $^{74}$Ge, $^{75}$As, $^{78}$Se, $^{95}$Mo, $^{107}$Ag, $^{111}$Cd, $^{113}$In, $^{115}$In, $^{118}$Sn, $^{121}$Sb, $^{125}$Te, $^{137}$Ba, $^{197}$Au, $^{202}$Hg, $^{205}$Tl, $^{208}$Pb and $^{209}$Bi. For Ge concentration $^{72}$Ge is used as main Ge isotope. For calibration the standards Mul-ZnS-1 (main standard; Onuk et al., 2016), MASS-1 (Wilson et al., 2002), UQAC-FeS-1 (LabMaTer, UQAC), UQAC-FeS-4 (LabMaTer, UQAC) and NIST612 (Wise and Wattens, 2012a) were used. Standards were analyzed at the start of the sequence and after every 40 sample spots. EMPA data of Cu (briartite, chalcopyrite, tennantite), Fe (pyrite, arsenopyrite), Zn (sphalerite) and Pb (galena) was used for internal calibration. For spots without available EMPA data (marked by asterisk in Supplementary Table 5), median contents of the respective elements and minerals of the EMPA dataset were used for internal calibration. Data reduction was conducted using the Iolite 3DRS plugin v.4.8.3 (Paton et al., 2011). Only flat intervals of the time count signal were considered for data reduction, but microinclusions could not always be completely avoided (e.g., Cu in sphalerite due to chalcopyrite disease). Due to isobaric interference of $^{115}$Sn on $^{115}$In and $^{113}$Cd on $^{113}$In, indium values in Sn- and Cd-rich minerals such as briartite are possibly overreported. Trace element concentrations of ore-hosted phengite and quartz was analyzed with the same equipment using a spot size of 35 μm, laser frequency of 10 Hz, fluence of 7.48 J/cm$^2$, He flow of 0.3 l/min (cell) and 0.2 l/min (cup), as well as Ar flow of 0.9 l/min and $N_2$ flow of 9 ml/min. The standards NIST612 (main), NIST614 (Wise and Wattens, 2012b), BIR-1G, BHVO-2G, and BCR-2G (all USGS) were used for calibration. For internal calibration the median Si content (48.02 wt%, EMPA data, Supplementary Table 3) was used for ore-hosted phengite and the ideal stoichiometric Si content of 46.74 wt% was used for quartz. The full dataset is available in Supplementary Table 5. Trace element concentrations are reported as median ± standard deviation.

### 3.5. Micro-XRF scanning

Micro-XRF (EDX) scanning of thin sections was carried out using a Bruker Tornado M4 micro-XRF at the Micro Analytical Laboratory of the Department of Applied Geochemistry at the Technical University of Berlin. An amplifying time per analysis spot of 30 ms, an acceleration voltage of 50 kV, a beam current of 600 μA and a beam size of 20 μm (spot distance 20 μm) were used for analysis. Data was processed with the M4 Tornado software. Resulting element maps are available in Supplementary Fig. 1.

## 4. Petrography

### 4.1. Host rocks

Host rocks to the mineralization at South Lakes Glacier consist of dolomite marble and metapelite. The marble is strongly foliated ($S_1$) with pronounced parallel layering striking roughly NW-SE (Fig. 4) and isoclinal folds. Dolomite is commonly granoblastic and shows shape preferred orientation with grain sizes of mostly 10 – 200 μm (Supplementary Fig. 2A, 2C). Twins are common (Supplementary Fig. 2B). Thin graphite schlieren are common in the marble, emphasizing the parallel layering (Supplementary Fig. 2C). Graphite forms thin flakes of 1—10 μm length with shape-preferred orientation. Calcite and pyrite occur as minor accessory phases. The marble is intercalated with meter-wide bands of fine grained, dark, graphitic, schistose metapelite consisting of quartz, phlogopite, phengite, alkali feldspar, graphite, pyrite and rutile (Supplementary Fig. 2D-F). Shape preferred orientation of phlogopite and phengite defines the foliation of the metapelite ($S_1$).

### 4.2. Ore textures at South Lakes Glacier

The mineralization at South Lakes Glacier is dominated by coarse, polymict, matrix-supported, chaotic to mosaic breccias with a massive sphalerite-dominated sulfide matrix and abundant angular to subrounded clasts (Fig. 4A-B). The clasts, consisting mainly of dolomite marble with minor amounts of metapelite and quartz aggregates, constitute a significant volume (20 – 25 %) of the massive sulfide ore (Fig. 4A–B). The clasts are between 1 – 50 cm in size with strong $S_1$-foliation, chaotic 3D orientation and strong internal deformation in the form of isoclinal to tight folds (Fig. 4A). Thin sulfide veinlets are emplaced along axial traces of isoclinal folds in clasts. The irregular sulfide breccia bodies crosscut $S_1$ foliation of the surrounding marble (Fig. 4B) and show tectonic thickening in fold hinges, forming saddle reef structures.

In addition to the breccia, mineralization occurs as extensional veins replacing marble along foliation planes, piercement veins and tension gashes (Fig. 4B–D). Arborescent sphalerite veins commonly extend from the sulfide breccias replacing surrounding marble (Fig. 4B). The orientation of the extensional veins is WNW-ESE (Fig. 4B–C, Rosa et al., 2023) and the tension gashes show a N-S to NE-SW trend (Fig. 4D), both consistent with $D_1$ NNE-SSW compression (Guarnieri and Baker, 2022). The sulfide breccia and associated vein mineralization post-date the onset of $S_1$ foliation and folding as evidenced by crosscutting relationships, clast foliation and clast-internal folds.

The main ore constituents are sphalerite, galena and pyrite, whereas chalcopyrite, arsenopyrite, tennantite, and briartite occur as minor sulfide phases (Fig. 5). Dolomite is the main gangue phase, with graphite, quartz, phengite, alkali feldspar, chlorite, calcite, rutile and apatite occurring as minor phases (Fig. 5). The mineralogy is more diverse than in the Black Angel mine (Horn et al., 2019). Four stages of mineralization were observed at South Lakes Glacier based on textures and spatial distribution (Fig. 5). Stage I is the main mineralization event and includes the major sulfides sphalerite, galena and pyrite, as well as briartite (Fig. 5). Stage I was affected by the main deformation event $D_1$. Stage II post-dates $D_1$ and is spatially limited. Stage III consists of galena and chalcopyrite fracture fills formed during the second deformation event $D_2$ post-dating stages I and II (Fig. 5). Stage IV consists of the supergene minerals anglesite, cerussite, covellite, goethite and smithsonite replacing primary ore minerals (Fig. 5). There is no observed difference in paragenesis between the studied samples.

### 4.3. Sphalerite

Sphalerite is the most common sulfide mineral and forms the matrix of the prevalent sulfide breccia (Fig. 4A, 6A–B). It is bright brown in outcrop and creamy yellow in transmitted light (Fig. 6A). Sphalerite mostly shows grain sizes of 100 – 600 μm but individual grains can reach up to 1 mm (Fig. 6C, 6H). Grains are anhedral showing a granoblastic amoeboid to granoblastic polygonal texture (Fig. 6C, 6E–F). Annealing twins are common (Fig. 6C, 6F, 6I). Deformation twins (Fig. 6G) and grain boundary bulging (Fig. 6H) occur occasionally. Sphalerite commonly occurs as roundish growth inclusions and embayments in pyrite-1 and pyrite-2 (Figs. 6I-J, 7D-E), and less commonly as irregular inclusions in dolomite and briartite (Fig. 8L). It can be found as crack-fill in pyrite-2 fractures together with galena and chalcopyrite-1. In several samples, sphalerite is fine-grained with grain sizes of 10 – 50 μm

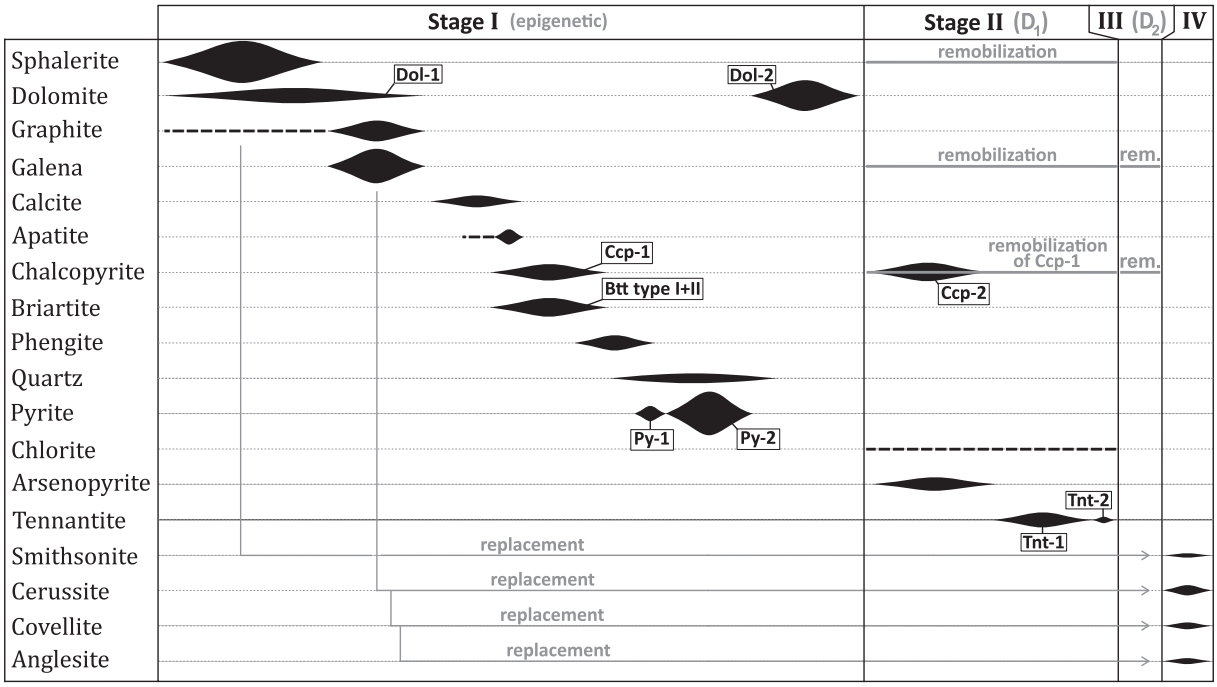


**Fig. 5.** Paragenetic sequence of the mineralization at South Lakes Glacier. The paragenesis is divided into four stages. Stage I corresponds to an epigenetic stage. It is affected by brittle-ductile deformation of $D_1$ resulting in sulfide remobilization. Stage II formed during $D_1$ and is affected in turn by $D_2$. Stage III consists of sulfides remobilized during $D_2$ and stage IV comprises late supergene minerals.

(Fig. 6E). These smaller grains show granoblastic polygonal texture and abundant annealing twins. Domains of finer-grained sphalerite coincide with more rounded pyrite-2 (Fig. 6D). In these domains larger sphalerite grains are preserved in pyrite growth embayments and in $D_1$ pressure shadows of pyrite (Fig. 6I).

### 4.4. Galena

Galena etched with a thiourea solution reveals a highly variable grainsize distribution from 50 μm to almost 2 mm. All galena grains are strongly granoblastic polygonal with 120° triple junctions (Fig. 7A). Galena forms coarse-grained aggregates and veinlets crosscutting sphalerite. Galena displays negative cuspate to curvilinear, corroded grain boundaries with sphalerite (Fig. 7A-B), but also with pyrite-2 and briartite, which can occur as rounded clasts in galena veinlets. It commonly exhibits cusp-and-caries replacement texture with sphalerite (Fig. 7B) and tends to accumulate in strain shadows of pyrite or wallrock clasts (Fig. 6D). It can also be found as injection veins in wallrock clasts along dolomite grain boundaries, and as small-scale fracture-fills in most other minerals, most notably in pyrite (Fig. 6K), tennantite (Fig. 7G, 7I), briartite (Fig. 8B, 8I) and sphalerite (Fig. 8B, 8E). Galena occurs as growth inclusions in pyrite-1 and pyrite-2 (Fig. 7F).

### 4.5. Chalcopyrite

Chalcopyrite is significantly less abundant than sphalerite, galena and pyrite. Chalcopyrite-1 is anhedral and ranges from 5 – 150 μm in size. It occurs as scattered grains in sphalerite (Fig. 7B), as grain trails (Fig. 8D) or as clusters in sphalerite (Fig. 7C). It also forms small, round inclusions in pyrite-1 and pyrite-2 (Fig. 7D), fills fractures in pyrite-2, and occurs in strain shadows of pyrite-2 and wallrock clasts. Chalcopyrite-1 often occurs together with and is locally intergrown with briartite (Fig. 8A). Chalcopyrite-2 is solely found in spatial association with arsenopyrite in galena veinlets and is intergrown with both arsenopyrite and galena (Fig. 7H, 7I). It forms anhedral grains of 50 – 200 μm. Fractures of tennantite-1 are locally filled by chalcopyrite-2 (Fig. 7I).

### 4.6. Briartite

Briartite [$Cu_2(Zn,Fe)GeS_4$] occurs in half of the ore samples and is more abundant at South Lakes Glacier compared to the Black Angel mine. Two different textures are distinguished: Type I briartite forms 50 μm to 3 mm large anhedral to subhedral grains or sub- to euhedral aggregates (Figs. 6B, 8B). Some type I grains are rounded to oval in sphalerite or galena matrix (Fig. 8C). Type II consists of anhedral, partly round to oval, <1 – 20 μm-sized grains occurring as clusters or isolated grains within sphalerite (Fig. 8D–G). Type II briartite grain clusters often resemble watermelon-type chalcopyrite disease (Figs. 7C, 8E).

Common micro-textures of type I briartite are growth and annealing twins (Fig. 8J, 8H). Larger grains locally have rims of smaller granoblastic grains growing at the expense of the larger grain (Fig. 8H). These recrystallized grains show grain boundary bulging recrystallization, 120° triple junctions, annealing twins and alignment along rims of parent grains (Fig. 8H). Type I briartite is riddled with round to elongate sphalerite, chalcopyrite and, less abundantly, tennantite inclusions (Fig. 8B, 8K, 8L). These inclusions follow crystallographic orientations of the host grain including twin planes. They show bimodal grain size distribution with a population of < 1 μm and a second population of 4 – 20 μm. The tennantite inclusions are 2 – 20 μm but are difficult to identify in the briartite matrix due to inconspicuous color. Some of the chalcopyrite inclusions show a core of elongate, worm-like sphalerite (Fig. 8K). The inclusions are crosscut by galena-filled fractures (Fig. 8I). Briartite grains occasionally exhibit flame-like exsolution patterns perpendicular to inclusion trails (Fig. 8K, Supplementary Fig. 3). This exsolution pattern is crosscut by the sphalerite, chalcopyrite and tennantite inclusions. Much larger, round to irregular growth inclusions of sphalerite, galena and dolomite do not follow crystallographic orientation (Fig. 8L). Type I briartite with abundant sphalerite inclusions occurs as inclusions in pyrite-2. Type II briartite grains do not show any

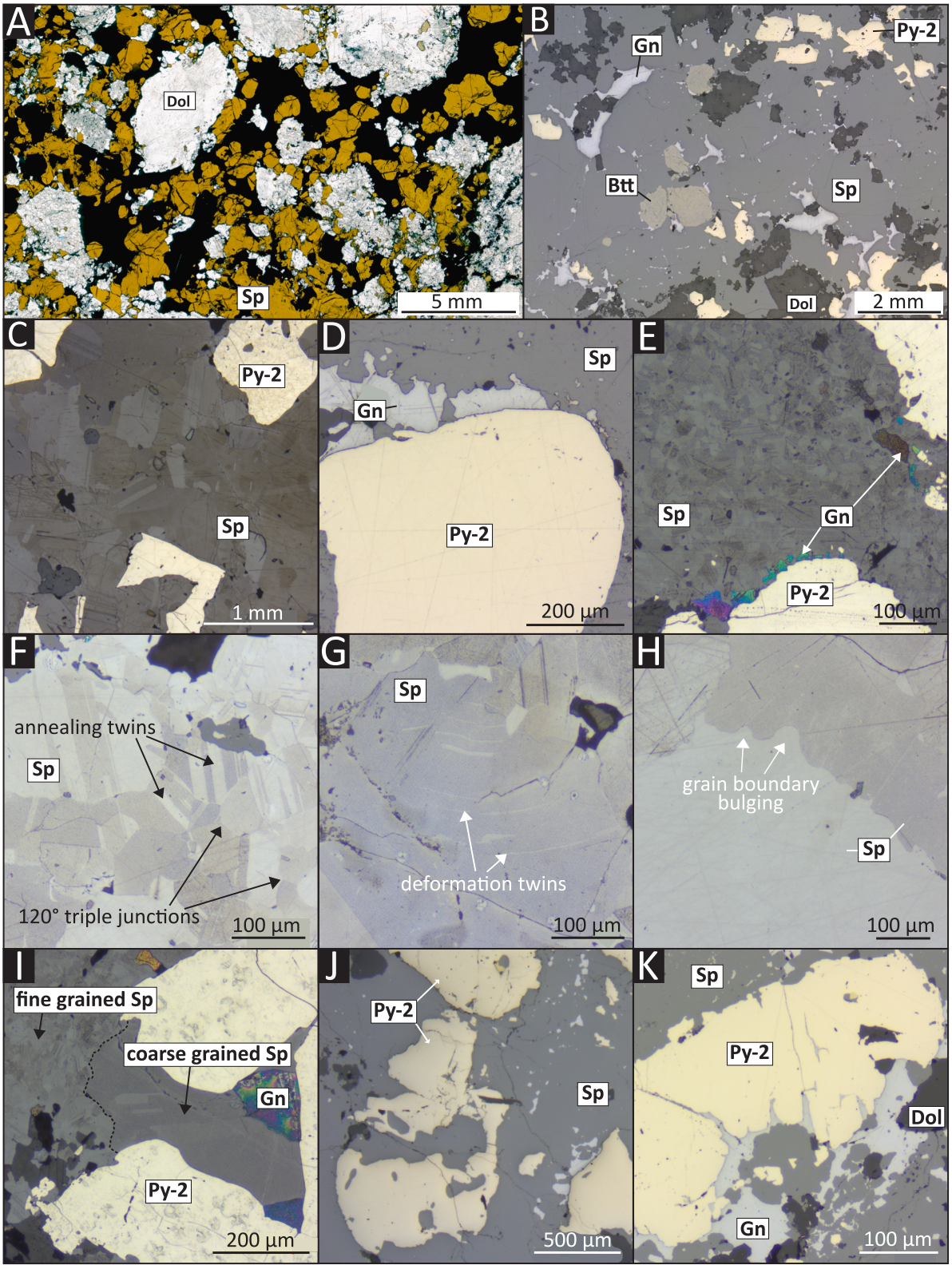


**Fig. 6.** Transmitted light thin section scans and reflected light microphotographs of sphalerite textures. Sphalerite in microphotographs C + E-I is etched with sodium hypochlorite [NaClO]. A) Thin section scan with yellow sphalerite (Sp) and dolomite (Dol). Pyrite and galena appear black. TL, PPL. Sample 561730B-2. B) Overview of mineralization with sphalerite, galena (Gn), briartite (Btt) and pyrite-2 (Py-2). RL, PPL. Sample 561732G. C) Coarse-grained, blocky sphalerite with subhedral pyrite-2. RL, PPL. Sample 561730B. D) Rounded pyrite-2 grain with galena accumulation in its pressure shadow. RL, PPL. Sample 561733. E) Fine-grained, equant, granoblastic sphalerite with abundant annealing twins. RL, PPL. Sample 561733. F) Annealing twins and 120° triple junctions in granoblastic sphalerite. RL, PPL. Sample 561731A. G) Thin, tapered and bent deformation twins in sphalerite. RL, PPL. Sample 561732A. H) Corse sphalerite grain with grain boundary bulging. RL, PPL. Sample 561730B. I) Coarser grained sphalerite preserved in pyrite-2 embayment, whereas sphalerite outside is fine grained. RL, PPL. Sample 561733. J) Anhedral to subhedral, poikilitic pyrite-2 grains overgrowing sphalerite. RL, PPL. Sample 561732I. K) Large, abraded and fractured pyrite-2 grain. Galena-1 (Gn-1) fills the fractures. RL, PPL. Sample 561733.

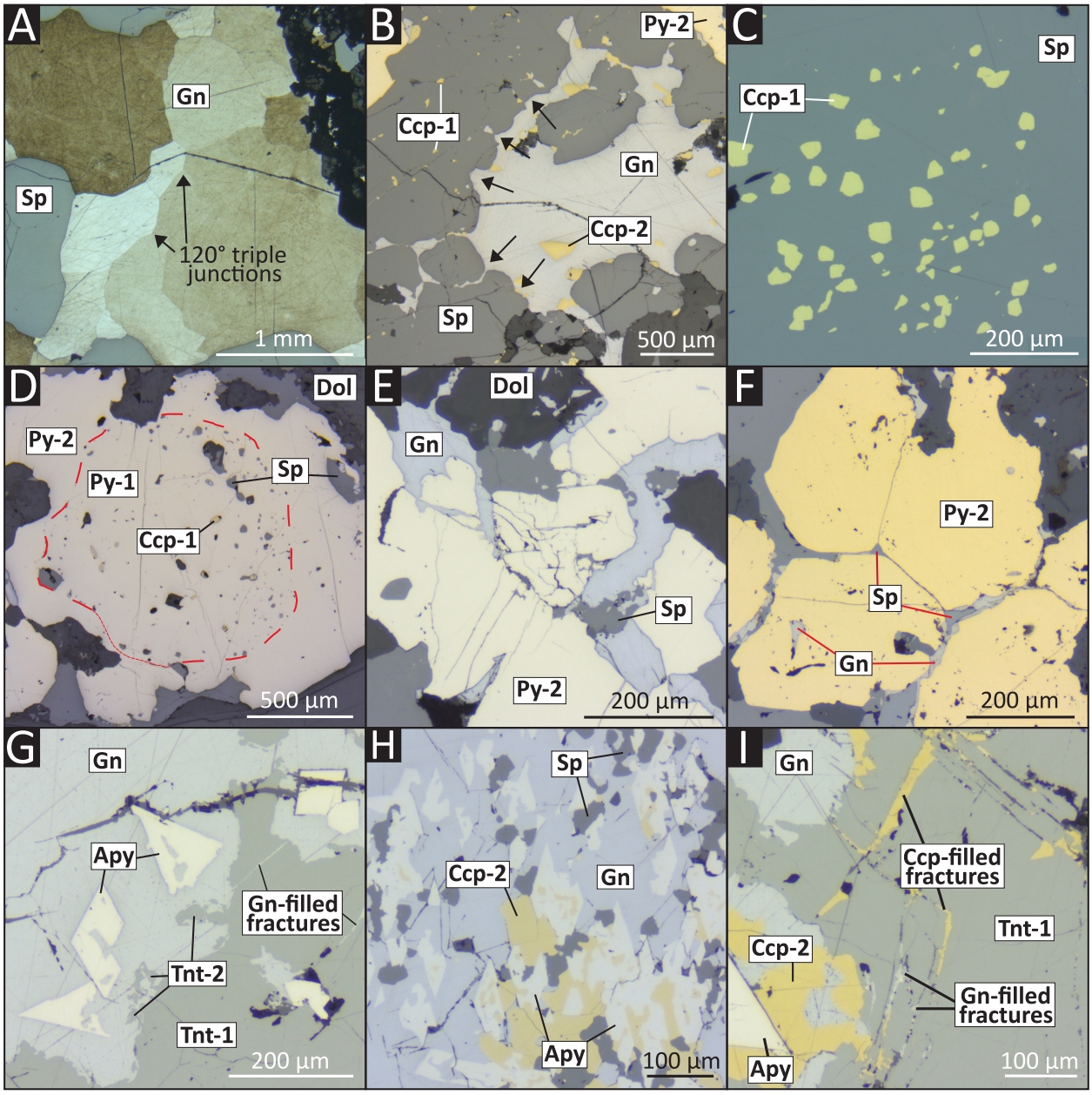


**Fig. 7.** Microphotographs of sulfide textures in reflected light. A) Coarse-grained, granoblastic galena (Gn). Galena was etched with a thiourea solution. RL, PPL. Sample 561730A-2. B) Cusp-and-caries replacement texture of remobilized galena and sphalerite (arrows). RL, PPL. Sample 561732B. C) Watermelon-type chalcopyrite disease in sphalerite (Sp). RL, PPL. Sample 561732F. D) Large, anhedral pyrite grain with inclusion-rich pyrite-1 (Py-1) core and inclusion-poor pyrite-2 (Py-2) rim. RL, PPL. Sample 561732A. E) Impingement cracking in pyrite-2 grains. RL, PPL. Sample 561730B. F) Sphalerite and galena filled 120° triple junctions in aggregate of annealed pyrite-2 grains. RL, PPL. Sample 561730B. G) Arsenopyrite (Apy), tennantite-1 (Tnt-1) and tennantite-2 (Tnt-2) intergrown with remobilized galena. Tennantite-1 shows thin galena-filled $D_2$-related fractures. RL, PPL. Sample 561732B. H) Arsenopyrite intergrown with chalcopyrite-2 and remobilized galena. RL, PPL. Sample 561732E. I) Tennantite-1 showing $D_2$-related fractures filled with either chalcopyrite or galena. Chalcopyrite-2 is intergrown with arsenopyrite and remobilized galena. RL, PPL. Sample 561732B.

inclusions (Fig. 8D–G). Twins and exsolution patterns are also absent. Briartite is intergrown with chalcopyrite-1 (Fig. 8A). Type II also occurs together with chalcopyrite-1 in grain trails, locally replacing chalcopyrite (Fig. 8D). It has been observed in sphalerite inclusions within pyrite-1 (Fig. 8G).

### 4.7. Pyrite

Pyrite grain size ranges from 100 µm to 2 mm but is mostly around 1 mm. Pyrite-1 occurs as relict cores overgrown by a rim of pyrite-2 (Fig. 7D). Grains with pyrite-1 cores are rare. Nearly all pyrite grains are poikilitic with abundant sphalerite inclusions (chadacrysts) and growth embayments along grain peripheries (Fig. 6J). These inclusions range from 50 – 400 µm in diameter. Dolomite, galena and (rarely) briartite form inclusions in pyrite-2. Inclusions in pyrite-1 cores are more abundant and of a greater mineralogical diversity, comprising sphalerite, galena, dolomite, quartz, chalcopyrite and feldspar (Fig. 7D). Pyrite-2 is anhedral to subhedral and locally shows abrasion, fracturing and impingement cracking (Figs. 6K, 7E). Fractures are filled by chalcopyrite-1, galena and sphalerite. Grain boundaries are usually rugged. Where in contact with galena, grain boundaries are often smooth and rounded. Where several pyrite grains form aggregates,

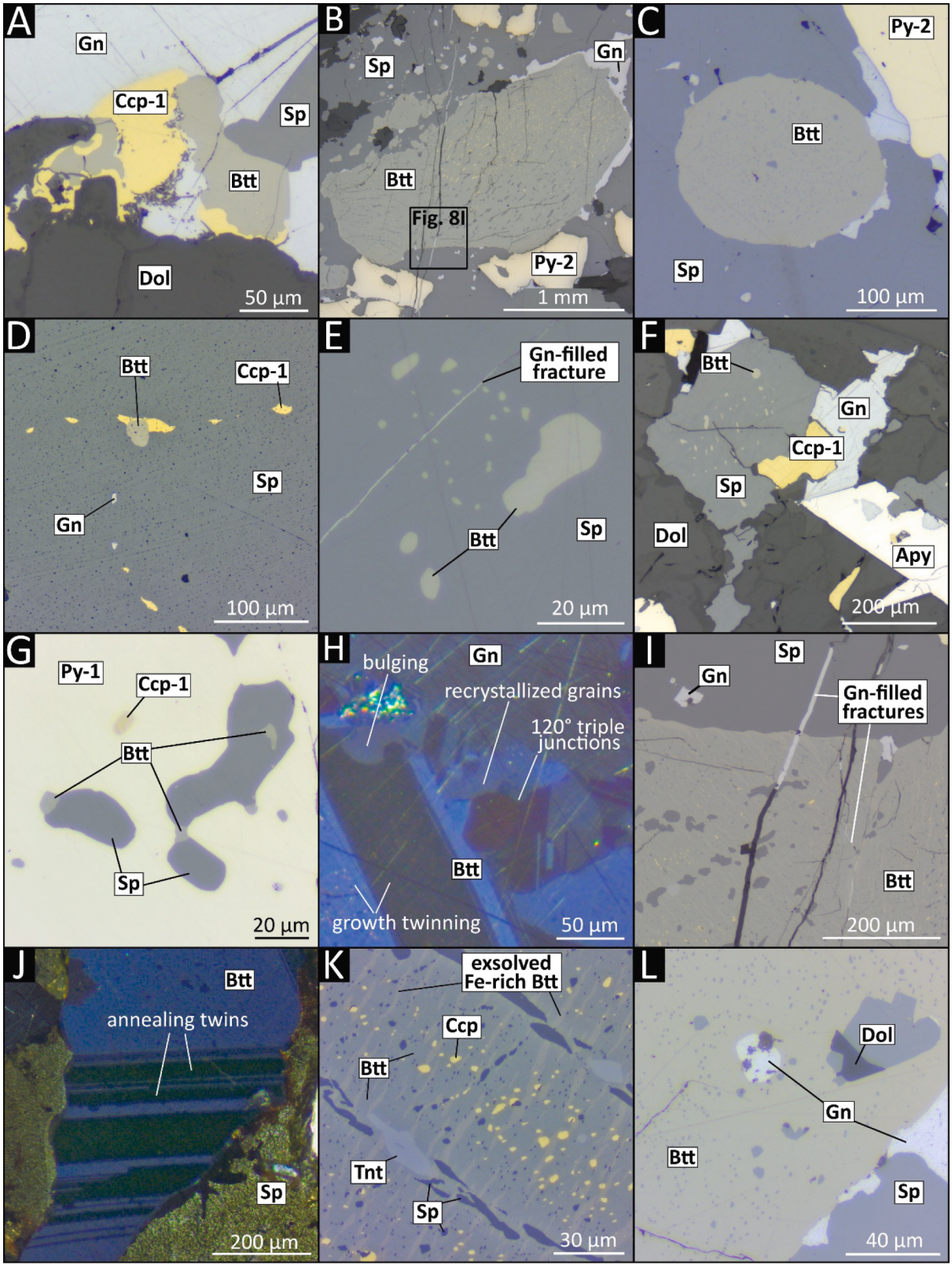


*(caption on next page)*

**Fig. 8.** Microphotographs of briartite textures. Samples are not etched. A) Type I briartite (Btt) intergrown with coeval chalcopyrite-1 (Ccp-1). RL, PPL. Sample BA1-B. B) Large mm-sized, sub- to anhedral type I briartite in galena (Gn) and sphalerite (Sp). Note the small sphalerite and chalcopyrite (Ccp) inclusions. Late $D_2$-related fractures crosscut the grain. RL, PPL. Sample 561732E. C) Rounded, abraded briartite grain (type I) with abundant small sphalerite inclusions in sphalerite matrix. RL, PPL. Sample 561731A. D) A type II briartite grain within a trail of chalcopyrite disease in sphalerite. RL, PPL. Sample BA1-B. E) Cluster of μm-sized, anhedral type II briartite in sphalerite matrix. A $D_2$-fracture filled by galena crosscuts sphalerite. RL, PPL. Sample 561730B. F) Cluster of μm-sized, anhedral type II briartite in sphalerite grain. RL, PPL. Sample 561730B. G) Type II briartite and sphalerite inclusions in pyrite-1 (Py-1). RL, PPL. Sample 561730B. H) Recrystallized briartite grains of 40 – 60 μm size with 120° triple junctions occur along the edge of coarse briartite type I grain. Grain boundary bulging was observed locally. Growth twins occur in the host grain. RL, XPL. Sample 561730A. I) Zoom-in of B. Galena-filled $D_2$-related fractures crosscut a large type I briartite grain as well as sphalerite inclusions therein. RL, PPL. Sample 561732E. J) Briartite (type I) with annealing twins. Twins have straight edges with local steps. RL, XPL. Sample 561730A. K) Sphalerite, chalcopyrite and tennantite (Tnt) inclusions in a large type I briartite grain. The sphalerite and chalcopyrite inclusions have a bimodal grainsize distribution. Larger sphalerite grains are elongate and oriented. A flame-like exsolution pattern of the briartite matrix is crosscut by the inclusions. RL, PPL. Sample 561732E. L) Type I briartite grain with small sphalerite inclusions overgrowing galena, sphalerite and dolomite, forming the respective larger inclusions. RL, PPL. Sample 561731A.

120 °C triple junctions are ubiquitous (Fig. 7F). Sphalerite and galena are observed as injections along triple junctions replacing pyrite (Fig. 7F).

### 4.8. Arsenopyrite

Arsenopyrite forms rhombic, euhedral grains between 30 – 400 μm (Fig. 7G – I). It is found almost exclusively in veinlets and patches of remobilized galena. Arsenopyrite commonly shows inclusions of galena and chalcopyrite-2 (Figs. 7G, 7H, 8F), and rarely inclusions of sphalerite and dolomite (Fig. 8F).

### 4.9. Tennantite

Tennantite is rare and forms large, mm-sized aggregates occurring solely in galena veinlets (Fig. 7G, 7I). Tennantite is partially intergrown with galena, resulting in galena inclusions and growth embayments. Chalcopyrite-2, arsenopyrite and galena occur as droplet-shaped patches within tennantite aggregates. The large aggregates mostly belong to tennantite-1, which show fractures filled by chalcopyrite and galena (Fig. 7G, 7I). Occasionally along tennantite-galena grain boundaries, a second generation of tennantite (Tnt-2) was observed (Fig. 7G). Tennantite-2 grains are very small (1 – 10 μm) and forms protuberances replacing galena.

### 4.10. Gangue minerals

The main gangue mineral is dolomite, which occurs in two generations with different textures. Dolomite-1 is abundant, forms aggregates with widely varying grain size between ~ 50 – 800 μm and commonly exhibits recrystallization and thick intersecting sets of twins. It overgrows sphalerite and often occurs as inclusions in pyrite-1 and pyrite-2. Dolomite-2 forms large, homogenous, anhedral grains and aggregates, that can reach a size of 3 – 4 cm. Graphite is commonly found as dark layers in the the marble but is also found as clusters in the massive sulfide ore. The elongate and curved grains are mostly < 10 μm in size, larger grains are rare. Graphite often forms symplectitic intergrowths with galena. Graphite can also be found as pockets in dolomite, and rarely, sphalerite. Apatite, forming small grains of 30 – 200 μm, is found in dolomite-1 aggregates, but has also been observed in galena, sphalerite and pyrite-2. Phengite occurs in the massive sulfide ore in the form of 50 – 400 μm sized euhedral laths in sphalerite and galena matrix. Phengite inclusions in pyrite-2 have been observed. Apatite and briartite locally occur as inclusions in phengite, and phengite and briartite are locally intergrown as well. Quartz forms large, rounded grains of 0.5 – 5 cm in diameter, visible as quartz 'eyes' in hand samples. These large grains show signs of strong abrasion. Quartz also forms 100 – 500 μm sized, anhedral grains and aggregates. Subgrains and subgrain rotation recrystallization are common. Foam texture has been observed in recrystallized grains. Chlorite forms rare aggregates of acicular, platy grains of 20 – 100 μm size and is hosted in remobilized galena.

## 5. Mineral chemistry

Major and trace elements of sulfides and micas were analyzed. All results, including apfu calculations, are reported in Supplementary Table 3 (EMPA) and Supplementary Table 5 (LA-ICP-MS). The major element data in weight percent is based on EMPA and the trace element data in parts per million is based on LA-ICP-MS. Values are reported here as range (min–max) and median ± standard deviation. Sulfide trace element contents are plotted in figure 9.

### 5.1. Sphalerite

The Fe content of sphalerite ranges from 0.4 – 2.9 wt% (2.0 ± 0.6 **wt** %) with the structural formula $Zn_{0.97}Fe_{0.04}S_{0.99}$ (n = 125, EMPA). The Cd content ranges from 2500 – 4500 ppm (3200 ± 350 ppm) and the Cu content from 140 – 3300 ppm (180 ± 110 ppm, n = 118). Several outliers with Cu values > 500 ppm are likely caused by chalcopyrite microinclusions. Manganese varies between 4 ppm and 380 ppm (220 ± 70 ppm) and Ga between 50 – 340 ppm (90 ± 30 ppm). Mercury has contents of 30 ± 30 ppm with values up to 120 ppm and Ag values are 12 ± 12 ppm (3 – 70 ppm). The Ge content is 5 ± 5 ppm (<1 – 27 ppm) with 18 % of Ge values below detection limit.

### 5.2. Galena

Cadmium ranges from 500 – 1400 ppm with a median of 800 ± 160 ppm (n = 74, EMPA). Silver shows contents of 180 ± 35 ppm and the Cu content is 730 ± 200 ppm (n = 27). The content of Tl is 420 ± 110 ppm, whereas the As content is 60 ± 40 ppm. Germanium is below the median detection limit of 21 ppm.

### 5.3. Chalcopyrite

Chalcopyrite-1 and chalcopyrite-2 show differences in trace element distribution. Due to small grainsize, only two analyses of chalcopyrite-1 are available. Chalcopyrite-1 has a Ge concentration of 630 ± 10 ppm (n = 2), whereas chalcopyrite-2 only has a concentration of 80 ± 110 ppm (n = 17). Gallium shows a similar distribution with 270 ± 10 ppm and 40 ± 20 ppm respectively, as well as Hg with 100 ± 10 ppm and 40 ± 20 ppm respectively, and Sn with 460 ± 10 ppm and 340 ± 110 ppm respectively. Arsenic is relatively low in chalcopyrite-1 with 45 ± 3 ppm and much higher in chalcopyrite-2 with 1170 ± 520 ppm.

### 5.4. Briartite

Major and trace element analysis of briartite was only conducted for type I briartite. The grain size of type II briartite, for which only one EMPA analysis is available, is too small for meaningful quantitative analysis. Briartite has a Ge content of 15.4 ± 0.4 wt% and an Sn content of 4.1 ± 0.5 wt% (Fig. 10, n = 76, EMPA). The composition is relatively Fe-rich with 12.6 ± 0.3 wt% Fe and 2.2 ± 0.8 wt% Zn (Fig. 10, EMPA). Due to the abundance of sphalerite and chalcopyrite inclusions it is not

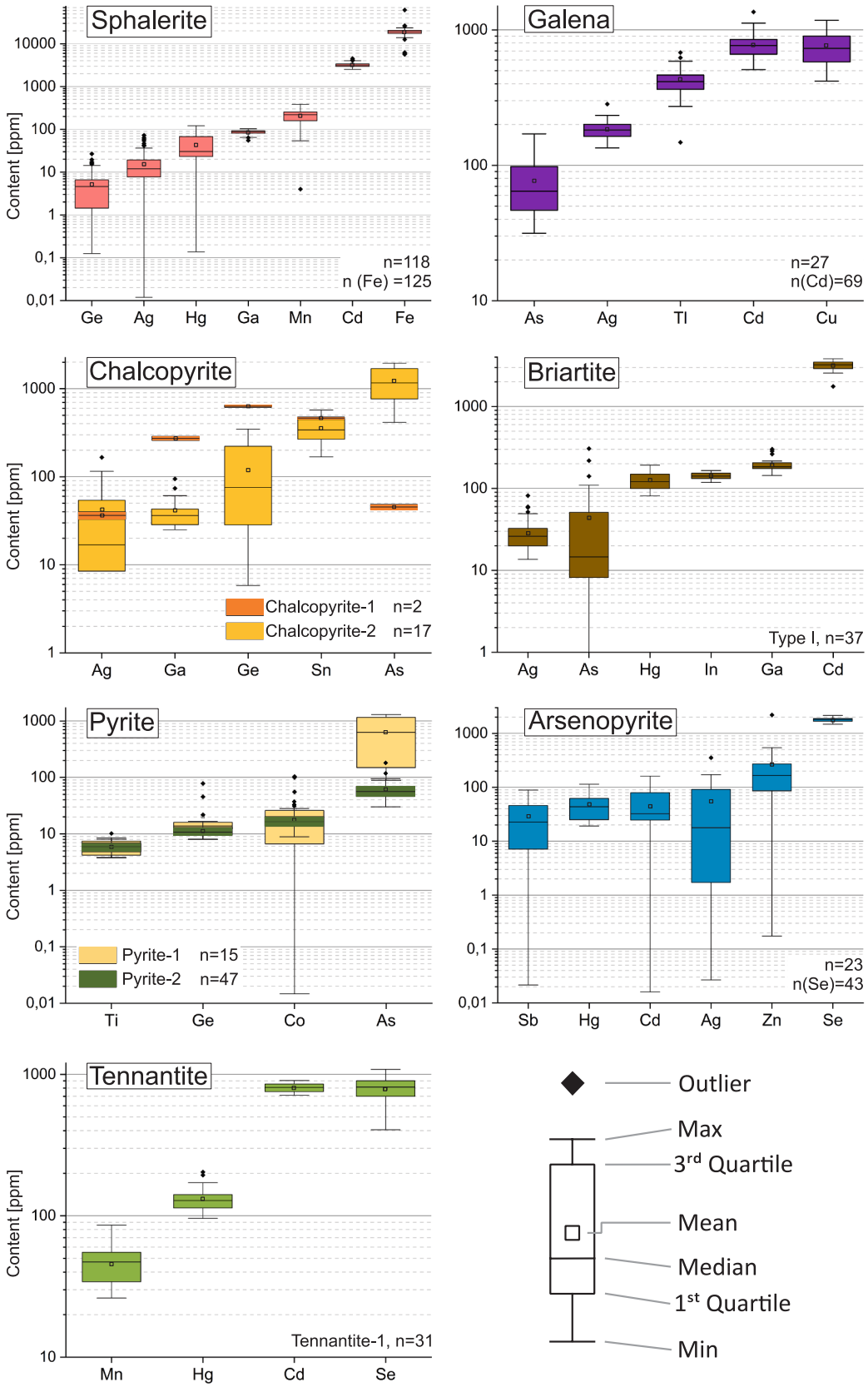


**Fig. 9.** Box and whisker plots of trace element data for sulfides from South Lakes Glacier (LA-ICP-MS data; EMPA data for Cd in galena, Se in arsenopyrite and Fe in sphalerite).

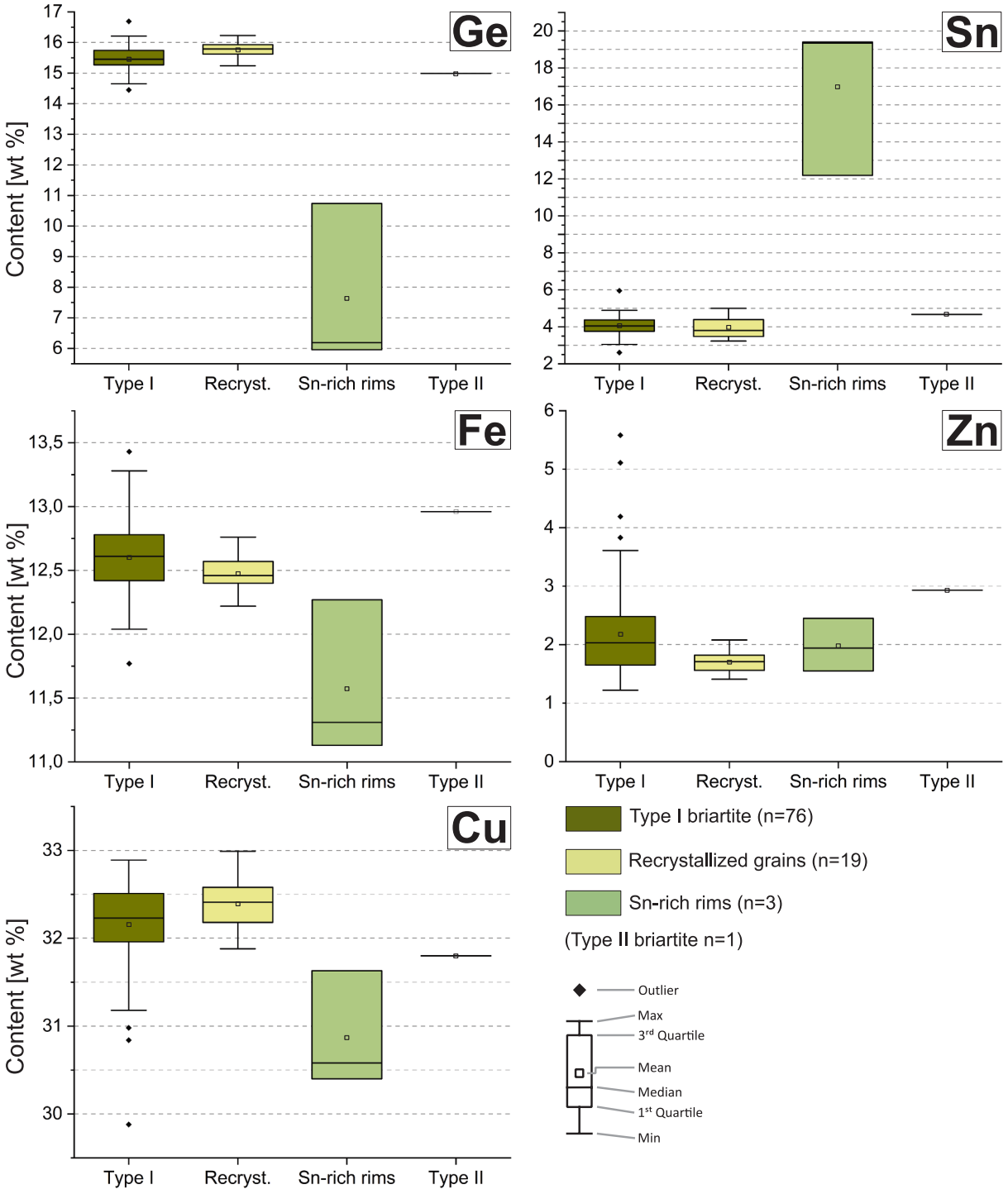


**Fig. 10.** Box-and-whisker plots of major element EMPA data (Ge, Sn, Fe, Zn, Cu) for different briartite texture types.

possible to rule out mixed analysis. The structural formula is $Cu_{2.01}(Fe_{0.90}Zn_{0.12})(Ge_{0.84}Sn_{0.14})S_{3.99}$. Smaller, anhedral briartite grains along rims of larger type I grains (Fig. 8H) have a lower Zn concentration of 1.7 ± 0.2 wt% (Fig. 10, n = 19, EMPA). Several briartite grains show rims of different composition, with strong enrichment in Sn and depletion of Ge, Fe and Cu (Fig. 10). The Sn content in these rims is 19.3 ± 3.4 wt% and the Ge content is 6.2 ± 2.2 wt% (Fig. 10, n = 3, EMPA). The structural formula of these rims is $Cu_{2.01}(Fe_{0.85}Zn_{0.12})(Sn_{0.68}Ge_{0.36})S_{3.95}$. No quantitative analysis is available for the flame-like exsolution pattern due to its small grainsize (Fig. 8K), however they show a more Fe-rich and Zn-poor composition than non-exsolved briartite in EDS mapping (Supplementary Fig. 3).

Significant trace elements in type I briartite are Cd, Ga, In, Hg, Ag and As (n = 37). The Cd content is 3200 ± 400 ppm (1800 – 3800 ppm). Cadmium in the Sn-rich rims is lower at 1500 ± 100 ppm (n = 3). Gallium shows values of 180 ± 30 ppm (140 – 300 ppm), Hg of 120 ± 30 ppm (80 – 190 ppm) and Ag of 25 ± 15 ppm (14 – 80 ppm). However, the high Ga content could not be reproduced by micro-XRF mapping (Supplementary Fig. 1). Arsenic ranges from 4 – 300 ppm (15 ± 60 ppm). This wide spread of As values can likely be explained by the presence of micro-inclusions of tennantite. Indium values of 150 ± 20 ppm ($^{113}$In) and 140 ± 10 ppm ($^{115}$In) have been measured. Due to

isobaric interference these In values are possibly overreported.

### 5.5. Pyrite

Pyrite-1 has an As content of 630 ± 450 ppm (90 – 1300 ppm, n = 15), whereas pyrite-2 has significant lower values of 60 ± 25 ppm (30 – 120 ppm, n = 47). The contents of other trace elements in pyrite is < 30 ppm, except for several outliers. The Ge content is 14 ± 18 ppm (8 – 78 ppm) in pyrite-1 and 11 ± 2 ppm (8 – 17 ppm) in pyrite-2.

### 5.6. Arsenopyrite

The As content of arsenopyrite is 42.9 ± 0.5 wt% (31.1 ± 0.4 at.%), the Fe content is 34.9 ± 0.3 wt% and the Se value is 0.2 ± 0.02 wt% (n = 40, EMPA). Zinc shows values of 170 ± 430 ppm (<1 –2200 ppm) and Ag values of 50 ± 90 ppm (<1 –350 ppm) (n = 23). The content of Hg is 45 ± 25 ppm (20 – 110 ppm), of Cd it is 30 ± 40 ppm (20 – 160 ppm) and of Sb it is 25 ± 25 ppm (<1 – 90 ppm). The In content is 10 ± 3 ppm.

### 5.7. Tennantite

Tennantite-1 has an As content of 19.2 ± 0.4 wt%, an Sb content of 0.5 ± 0.5 wt% and a Ag content of 1.3 ± 0.15 wt% (n = 64, EMPA). The structural formula is $(Cu_{9.94}Ag_{0.17})(Fe_{1.16}Zn_{0.81})(As_{3.84}Sb_{0.07}Cd_{0.01})(S_{12.98}Se_{0.02})$. Tennantite-2 has a lower As content of 14.3 ± 1.5 wt% but has a higher Sb content of 7.6 ± 2.2 wt% and Ag content of 2.7 ± 0.6 wt% (n = 6, EMPA). The Cd content is 800 ± 80 ppm and Se content is 530 ± 150 ppm (n = 6, EMPA). The structural formula is $(Cu_{9.69}Ag_{0.39})(Fe_{0.94}Zn_{0.99})(As_{2.97}Sb_{0.97}Cd_{0.01})(S_{12.99}Se_{0.01})$. Tennantite inclusions in briartite show As values of 18.9 ± 0.1 wt%, Sb values of 1.1 ± 0.4 wt% and Ag values of 2.1 ± 0.1 wt% (n = 2, EMPA). The formula is $(Cu_{9.70}Ag_{0.29})(Fe_{1.68}Zn_{0.50})(As_{3.77}Sb_{0.14})(S_{12.92}Se_{0.01})$.

The trace element contents of tennantite-1 are: Cd, 600 ± 150 ppm; Se, 800 ± 150 ppm; Hg, 130 ± 25 ppm; and Mn, 50 ± 10 ppm (n = 31). Other trace elements like Ge, Ga, In and Sn are < 10 ppm. Due to small grain size no trace element data is available for tennantite-2 and the tennantite inclusions in briartite.

### 5.8. Phengite and quartz

The structural formula of wallrock-hosted phengite is $(K_{0.97}Na_{0.03})(Al_{1.74}Mg_{0.14}Fe_{0.06}\ Ti_{0.06})(Si_{3.15}Al_{0.85})\ O_{10}(OH)_2$. The formula for ore-hosted phengite is $(K_{0.98}Na_{0.02})(Al_{1.78}Mg_{0.11}Ti_{0.04})(Si_{3.23}Al_{0.77}O_{10}[(OH)_{1.98}F_{0.02}]$. Fluorine is below detection limit in wallrock-hosted phengite (n = 20), but ranges from 0.03 – 0.33 wt% with a median of 0.1 ± 0.1 wt% in ore-hosted phengite (n = 52, EMPA, Supplementary Table 3). Qualitative micro-XRF mapping revealed an association of Ge with ore-hosted phengite and quartz (Fig. 11). Ore phengite has a Ge content of 660 ± 450 ppm ranging from 300 – 1900 ppm and a Ga content of 250 ± 200 ppm ranging from 90 – 690 ppm (n = 54, Supplementary Table 5). The Cu concentration is 1 ± 16 ppm (<1 – 80 ppm).

The Ge concentration of quartz is 370 ± 170 ppm (6 – 560 ppm), with one grain showing much lower values of 13 ± 2 ppm (n = 31, Supplementary Table 5). The Ga content is 1 ± 6 ppm (1 – 22 ppm). Phengite and quartz do not contain any Ge-bearing microinclusions (Supplementary Fig. 4).

### 5.9. Whole rock analysis

The sulfide breccia at South Lakes Glacier shows mean whole rock Zn values of 27.1 ± 3.5 wt% and Pb values of 6.7 ± 1.2 wt% (n = 3, ICP-MS, Supplementary Table 1). Mean Cd values are 1700 ± 210 ppm (1410 – 1940 ppm) and the Mn content is 350 ± 34 ppm (298 – 373 ppm).

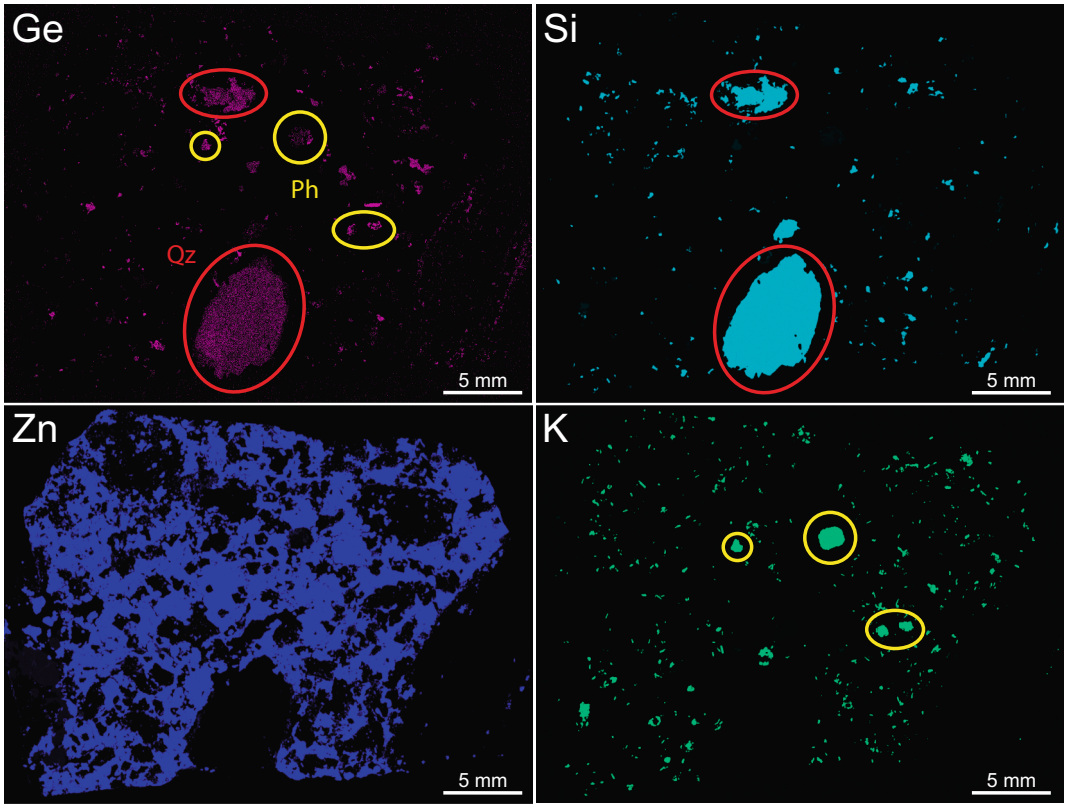


**Fig. 11.** Micro-XRF scans showing the distribution of Ge, Si, Zn and K in sample 561732B. Briartite is absent in this sample. Germanium is not associated with sphalerite (represented by Zn), which is homogeneously barren of Ge. Germanium shows an association with Si and K, corresponding to quartz (Qz, red circle) and phengite (Ph, yellow circle).

Copper ranges from 302 – 971 ppm (530 ± 317 ppm). The mean Ga content is 130 ± 13 ppm (111 – 138 ppm) and the mean Ge content is 120 ± 27 ppm (99 – 158 ppm). The mean values of Ag are 25 ± 6 ppm (19 – 32 ppm) and In values are 0.6 ± 0.1 ppm (0.5 – 0.7 ppm).

## 6. Geothermobarometry

### 6.1. Graphite thermometry

Graphite hosted in dolomitic marble, as well as in sphalerite, has been analyzed by Raman spectroscopy. Evaluation of graphite Raman spectra with the IFORS software (Lünsdorf and Lünsdorf, 2016) yields metamorphic temperatures ranging from 470 – 540 °C with a median of 510 ± 40 °C (Supplementary Table 4, n = 45), including the random uncertainty of graphite thermometry of 36—37 °C. The average temperature of grains hosted in dolomite marble and ore is similar within error, but only one ore-hosted grain was analyzed.

### 6.2. Arsenopyrite thermometry

The arsenopyrite geothermometer by Kretschmar and Scott (1976) is applied to euhedral arsenopyrite. Textural evidence shows that arsenopyrite is in equilibrium with pyrite (Supplementary Table 4). Arsenopyrite was buffered by pyrite alone, as neither pyrrhotite nor löllingite are present. This thermometer yields a temperature of 390 ± 30 °C (Supplementary Table 4). Arsenopyrite shows an intermediate sulfur fugacity with a mean $\log_{10}fS_2$ of −7.2 ± 1.2 (Supplementary Table 4; Sharp et al., 1985).

### 6.3. Biotite thermometry

The biotite thermometer (Henry, 2005; Wu and Chen, 2015) is calibrated for rutile- and/ or ilmenite-bearing, $TiO_2$-saturated, graphitic metapelite and P-T ranges of 0.1 – 1.9 GPa and 450 – 840 °C. Biotite thermometry was applied to phlogopite from graphitic, rutile-bearing metapelites of the Mârmorilik Formation from the South Lakes Glacier area (Supplementary Table 4). The metapelite was sampled in proximity to, but outside of, massive sulfide mineralization. Phlogopite follows regional $S_1$ foliation. The calculated median temperature after Wu and Chen (2015) is 530 ± 65 °C (Supplementary Table 4, n = 67) based on a pressure of 1.5 kbar (Pedersen, 1980). A temperature of 510 ± 25 °C is estimated after Henry (2005) (Supplementary Table 4, n = 67).

## 7. Discussion

### 7.1. Metamorphic temperature history

Temperatures reconstructed with the graphite thermometer (510 ± 40 °C) together with the biotite thermometer (530 ± 65 °C and 510 ± 25 °C) show peak upper greenschist to lower amphibolite facies conditions for Rinkian metamorphism. These results are in line with the estimated peak temperature of ~ 500 °C for the Angel orebody based on the metamorphic mineral assemblage (Pedersen, 1980). Microstructures at South Lakes Glacier indicate similar peak temperatures. Dolomite twins form at temperatures > 300 °C (Barber et al., 1981) and subgrain rotation recrystallisation of quartz indicates temperatures of ~ 400 – 500 °C (Stipp et al., 2002). The arsenopyrite thermometer of Kretschmar and Scott (1976) is generally considered valid for ores formed under greenschist and amphibolite facies conditions (Sharp et al., 1985). The thermometer yields a temperature of 390 ± 30 °C (Supplementary Table 4) which is significantly lower than the peak metamorphic temperature determined by graphite and biotite thermometry. Arsenopyrite is a robust mineral and unlikely to be reset by deformation (Fougerouse et al., 2016). Therefore, this temperature could reflect prograde or retrograde growth of arsenopyrite.

### 7.2. Timing and relationship of mineralization and deformation

Ore stage I, comprising the main part of the mineralization at South Lakes Glacier, formed around 1884 ± 35 Ma as indicated by Re-Os ages of ore pyrite from Black Angel, equivalent to pyrite-2 in this study, and therefore represents an epigenetic MVT mineralization (Fig. 12, Saintilan et al., 2024). During the Rinkian orogeny $D_1$ deformation lead to mechanical/solid-state (plastic flow) and fluid-assisted (dissolution-reprecipitation) remobilization of ore stage I (Fig. 12). Remobilization refers to translocation and redistribution of pre-existing sulfides (Marshall and Gilligan, 1993). At amphibolite facies metamorphic conditions, as determined by various geothermometers for the Rinkian orogeny, many of the common sulfides will be ductile (e.g. sphalerite, galena, chalcopyrite), whereas wallrock and competent ore minerals (e.g. pyrite) will still behave brittle, creating a contrast in rheological behavior essential for mechanical remobilization (Marshall and Gilligan, 1993). The massive sulfide breccia at South Lakes Glacier has been interpreted as either deformed pre-orogenic dissolution collapse breccia (Partin et al., 2021; Rosa et al., 2023) or as syn- to post-tectonic breccia (Horn et al., 2019). Strongly folded marble clasts within the sulfide breccia at South Lakes Glacier (Fig. 4A–B) imply that breccia formation occurred after the onset of regional deformation, as strain partitioning into the much weaker sulfide matrix likely prevents folding of the clasts after being embedded in the sulfides (Marshall and Gilligan, 1993; Tomkins, 2007). The sulfide bodies clearly crosscut $S_1$ foliation of the wallrock and the orientation of sulfide veins and tension gashes are consistent with $D_1$ (Fig. 4). The breccia at South Lakes Glacier was therefore formed by sulfide remobilization during $D_1$, like parts of the Angel orebody (Pedersen, 1980, 1981). Such breccias with ductile sulfide matrix and competent clasts (durchbewegung texture) are a typical macroscale feature of metamorphosed massive sulfide deposits formed by solid-state remobilization processes (Denisová et al., 2023; Gilligan and Marshall, 1987; Marshall and Gilligan, 1987; Vokes, 1969). Piercement veins are another indicator of solid-state remobilization of sulfides by plastic flow, particularly of sphalerite (Fig. 4C). At the microscale, brittle clasts, such as pyrite and quartz, locally experienced cataclasis, resulting in fracturing, fragmentation (Figs. 6K, 7E) as well as rotation and abrasion, evidenced by round quartz ‘eyes’ (Figs. 4, 6D). Brittle dolomite marble clasts were less affected, mostly retaining an angular shape. Galena was remobilized into small veinlets crosscutting the massive sulfide. Chalcopyrite-1 and galena also accumulated in pressure shadows of pyrite grains (Fig. 6D). In addition to solid-state processes, fluid-state remobilization affected sphalerite, galena and chalcopyrite. Sphalerite-filled tension gashes (Fig. 4D), arborescent sphalerite veins extending from the breccias (Fig. 4B), as well as sulfide-filled fractures and triple junctions in pyrite (Figs. 6K, 7F) formed by localized dissolution-precipitation (Gilligan and Marshall, 1987; Skinner and Johnson, 1987; Zheng et al., 2012).

Sphalerite and briartite show evidence of dynamic recrystallization with bulging grain boundaries (Figs. 6H, 8H) and relic deformation twins (Fig. 6G). Recrystallization led to pervasive grain size reduction in discrete zones within the ore (Fig. 6E), where coarser sphalerite was protected by pyrite embayments (Fig. 6I) and pyrite grains are abraded (Fig. 6D). This implies strain localization into these zones.

Ore stage II consists of minerals, that occur only within remobilized galena and are intergrown with galena. This indicates that stage II minerals formed during or after remobilization of galena. Arsenopyrite thermometry thus possibly represents the temperature of galena remobilization either during prograde or retrograde metamorphism. Near peak and retrograde remobilization has been suggested for other metamorphosed deposits (Cook et al., 1993; Craig et al., 1998; Vikentyev et al., 2016). Chlorite, a typically retrograde mineral, was observed intergrown with galena. Thus, remobilization at South Lakes Glacier likely occurred during retrograde metamorphism. Galena stays mobile at lower temperatures than the other sulfides, meaning that remobilization of sphalerite and chalcopyrite may have occurred at higher

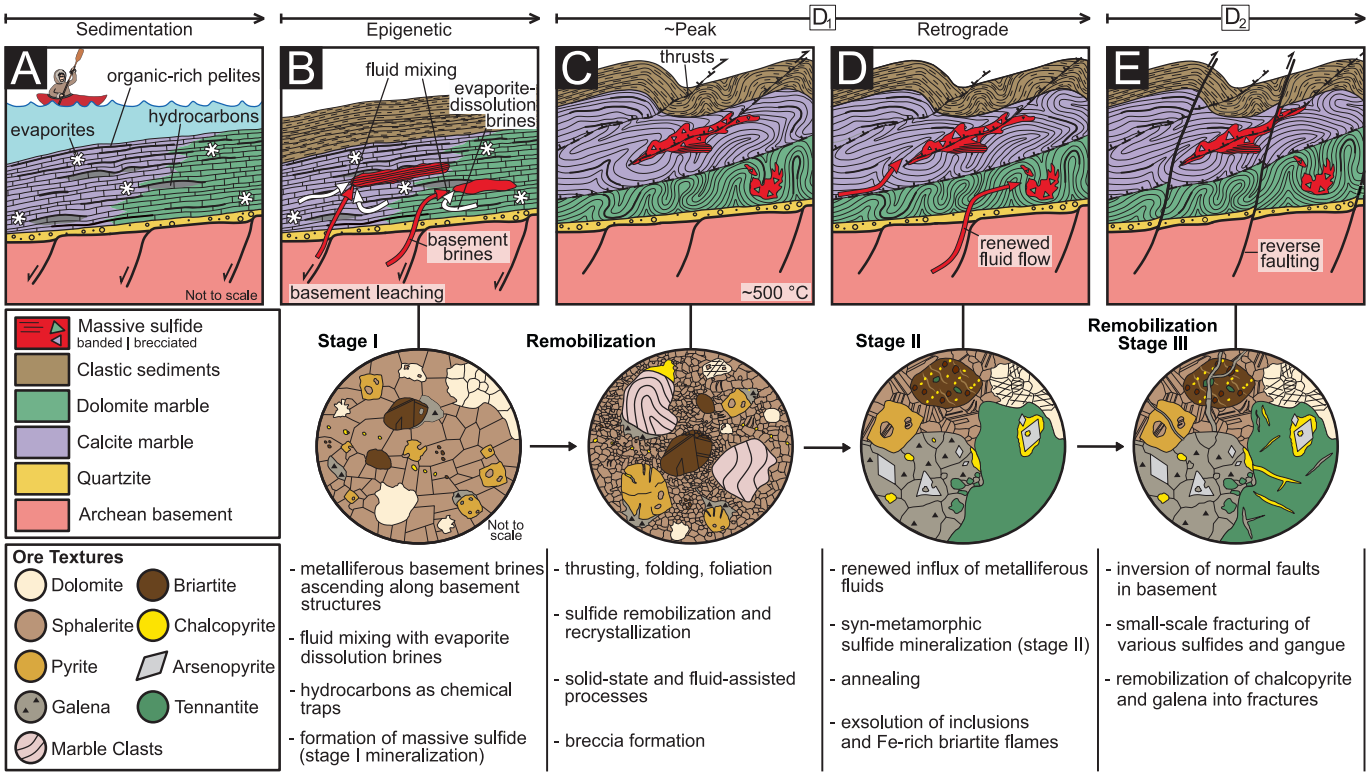


**Fig. 12.** Schematic model of ore genesis in the Black Angel district and associated ore textures. A) Formation of the Mârmorilik Formation as evaporite and hydrocarbon bearing carbonate platform. B) Epigenetic MVT mineralization (stage I) by rising metalliferous basement brines mixing with sulfate-bearing evaporite-dissolution brines and hydrocarbon-derived fluids. C) The area is affected by thrusting and folding during the Rinkian orogeny ($D_1$). Sphalerite, galena and chalcopyrite are remobilized and massive sulfide breccias are formed. D) During retrograde metamorphism rising metalliferous fluids lead to stage II mineralization. Sulfides are annealed and exsolution textures form in briartite. E) During $D_2$, reverse faulting leads to fracturing of sulfides and remobilization of galena and chalcopyrite into these fractures (stage III).

temperatures closer to peak conditions (Marshall and Gilligan, 1987). Stage II is interpreted to have formed from retrograde metamorphic fluids. Syn-metamorphic modification of the ore by renewed influx of metalliferous (As, Cu) fluids is supported by a *syn*-metamorphic Re-Os age of 1828 ± 17 Ma for wallrock pyrite from Black Angel (Saintilan et al., 2024). Therefore, ore stage II is likely significantly younger than ore stage I.

Small-scale brittle fractures crosscutting various sulfides, e.g. sphalerite (Fig. 8B, 8E, 8I), briartite (Fig. 8B, 8I) and tennantite (Fig. 7G, 7I), that are filled by remobilized sulfides (ore stage III), likely formed during brittle $D_2$ deformation, as these fractures post-date ore stages I and II, and crosscut annealed sulfide grains (Fig. 12). The galena and chalcopyrite fracture fill formed most likely by closed system fluid-state remobilization and dissolution-precipitation processes (Gilligan and Marshall, 1987; Zheng et al., 2012).

Widespread granoblastic textures and abundant annealing twins of sphalerite (Fig. 6E–F), galena (Fig. 7A), briartite (Fig. 8H, 8J), pyrite (Fig. 7F), quartz and dolomite indicate that the ore was well annealed. Annealing overprinted and most likely erased a large part of deformation fabric in the sulfides (Gilligan and Marshall, 1987). Annealed grains do not show an overprint of dynamic recrystallization but are crosscut by the $D_2$-related sulfide-filled fractures. Therefore, annealing likely postdates $D_1$ and predates $D_2$. Due to complete recrystallization sphalerite appears to be in equilibrium with other sulfides, such as galena and pyrite, that it did not form coevally with.

### 7.3. Mechanisms of briartite formation

Possible mechanisms for briartite formation encompass: (1) liberation of Ge during sphalerite recrystallisation and subsequent *syn*-metamorphic growth of distinct Ge minerals (Cugerone et al., 2021; Cugerone et al., 2020; Fougerouse et al., 2023); (2) precipitation from Ge-bearing (meta-)hydrothermal fluids, as for example at the Kipushi deposit (Kampunzu et al., 2009) or at Khusib Springs (Melcher, 2003); and (3) briartite exsolution from Ge-rich chalcopyrite (Kabwe deposit; Kamona and Friedrich, 2007). Briartite in KPT deposits commonly forms round to oval, μm-sized inclusions in sphalerite, galena and pyrite (Belissont et al., 2016; Höll et al., 2007; Kamona and Friedrich, 2007; Kampunzu et al., 2009). Briartite textures reported from the Angel orebody are similar to those from KPT deposits, but with a larger grain size (Horn et al., 2019). However, type I briartite textures observed in this study are distinctly different. Type I briartite is much larger (up to 3 mm) than what has been described from other briartite-bearing deposits (De Vos et al., 1974; Intiomale and Oosterbosch, 1974; Kamona and Friedrich, 2007; Kampunzu et al., 2009; Cugerone et al., 2020). Germanium-sulfides formed by sphalerite recrystallization and exsolution from chalcopyrite are much smaller than their parent sphalerite or chalcopyrite grains, typically < 20 μm (Cugerone et al., 2018; Fougerouse et al., 2023; Kamona and Friedrich, 2007). At South Lakes Glacier briartite I grains are significantly coarser than sphalerite. Sphalerite has a homogenous Ge distribution without Ge-enriched remnants, and a consistently low Ge concentration (~5 ppm) compared to sphalerite in many other Zn-Pb deposits (Figs. 9, 11). The high Ge concentrations of phengite and quartz show that Ge was present in the hydrothermal fluid. Moreover, type I and II briartite occur as growth inclusions in pyrite-1 and pyrite-2 (Fig. 8G), indicating that briartite formed prior to pyrite-2, which was dated at 1884 ± 35 Ma (Re-Os age; Saintilan et al., 2024). Thus, (1) the larger grain size of briartite than sphalerite; (2) the lack of Ge-rich sphalerite remnants; (3) the spatial association of briartite with other minerals than sphalerite; (4) the high Ge

concentration in coeval phengite and (5) the occurrence of type I and II briartite within early-stage pyrite-2 indicate that type I briartite formed by precipitation from a Cu-Ge-bearing hydrothermal fluid.

Type II briartite (Fig. 8D–G), and similar briartite from Black Angel (Horn et al., 2019), resemble briartite formed by sphalerite recrystallization (Cugerone et al., 2020). However, these grains do not occur in ribbons or patches of recrystallized sphalerite, but rather as clusters or isolated grains, and are not systematically associated with recrystallized sphalerite. It is therefore unlikely that type II briartite formed by sphalerite recrystallization. However, due to the occurrence of type II briartite in trails of chalcopyrite disease (Fig. 8D) and the resemblance of clusters with watermelon-type chalcopyrite disease (Fig. 7C, 8E–F), type II briartite may have formed analogously as'briartite disease' through reaction of a Cu-Ge-bearing fluid with the host sphalerite. A similar texture of 1 – 5 μm sized clustered briartite grains in sphalerite matrix has been described from the Kipushi mine, indicating that 'briartite disease' may not be limited to the Black Angel district (Francotte et al., 1965; Intiomale and Oosterbosch, 1974).

Similar minute inclusions of sphalerite and chalcopyrite within briartite as observed at South Lakes Glacier have also been reported from Kipushi, Kabwe and Black Angel (De Vos et al., 1974; Kamona and Friedrich, 2007; Horn et al., 2019). Crystallographically oriented chalcopyrite inclusions in briartite at Kipushi are interpreted as exsolution (De Vos et al., 1974), whereas a similar texture from the Kabwe deposit was interpreted as the result of simultaneous growth of briartite and chalcopyrite (Kamona and Friedrich, 2007). Briartite can incorporate a significant amount of As, e.g. up to ~ 0.95 wt% at Kipushi (Kampunzu et al., 2009). Briartite at South Lakes Glacier, however, has a low mean As concentration of 15 ppm (Fig. 9). Tennantite inclusions in briartite thus likely formed by exsolution, depleting the host in As. Sphalerite and chalcopyrite inclusions may have formed in a similar way by using excess Zn, Cu and Fe. The inclusions were then concentrated along twin boundaries by intragranular diffusion/dislocation-impurity pair diffusion, as twin boundaries commonly contain a high number of dislocations (Kelly and Knowles, 2012; Piazolo et al., 2016; Vukmanovic et al., 2014). Smaller, granoblastic briartite grains along rims of larger type I grains (Fig. 8H) formed by recrystallization, as evidenced by grain boundary bulging, 120° triple junctions and annealing twins. These grains have a lower median Zn content than its parent (Fig. 10) and lack sulfide inclusions. This indicates that excess Zn and other metals were expelled from briartite during dynamic recrystallization before exsolution of sphalerite, chalcopyrite and tennantite could occur. The flame-like exsolution pattern (Fig. 8K) formed prior to the minute inclusions, as it is crosscut by inclusion trails. In several briartite grains, $D_2$ fractures filled by remobilized galena (Fig. 8I) crosscut the inclusions and exsolution flames, indicating that exsolution occurred prior to $D_2$, likely during the retrograde stage of $D_1$.

### 7.4. Germanium distribution in the ore

In most Zn-Pb deposits Ge is hosted in sphalerite (Frenzel et al., 2016). South Lakes Glacier is clearly an exception with a relatively low Ge content of sphalerite and briartite as the main Ge host. A likely explanation for this discrepancy is differences in physicochemical conditions of the mineralizing fluids. It has been suggested that Ge is preferentially substituted into sphalerite at low to intermediate sulfur activity levels but enters discrete Ge-sulfides and sulfosalts in higher sulfur activity or high Cu environments (Fig. 13; Bernstein, 1985). This effect can be observed in various deposit types, e.g. Kipsuhi-type and epithermal deposits (Bogdanov et al., 2004; Höll et al., 2007; Melcher, 2003; Paar and Putz, 2005; Sahlström et al., 2017). The temperature of ore fluids in the Black Angel district is unknown, but assuming typical fluid temperatures of MVT deposits (<250 °C) the low Fe content of sphalerite (~2 wt%) as well as the coexistence of pyrite and chalcopyrite suggest an intermediate sulfur activity level for South Lakes Glacier (Einaudi et al., 2003). This would shift to a higher sulfur activity when

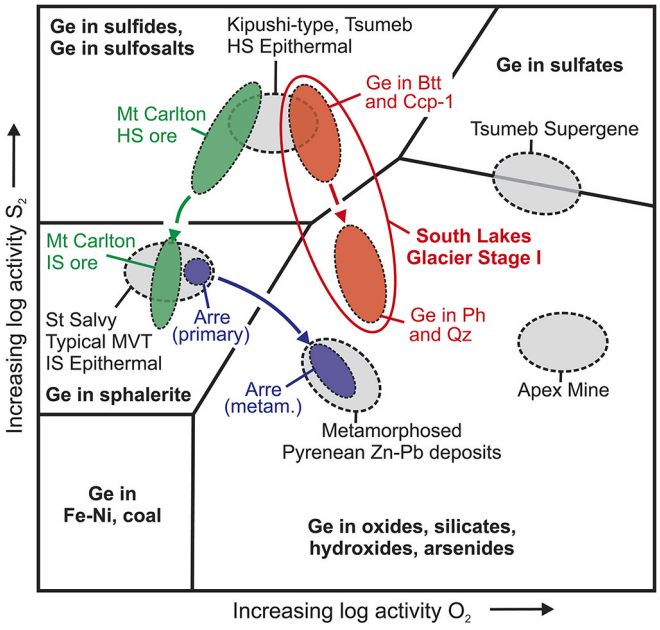


**Fig. 13.** Relative $S_2$-$O_2$ activity diagram showing Ge behaviour in different geochemical environments, modified after Bernstein (1985). Ore stage I at South Lakes Glacier transitions from Ge in sulfides to Ge in silicates as evidenced by briartite (Btt) and Ge-bearing chalcopyrite-1 (Ccp-1) followed by Ge-bearing phengite (Ph) and Ge-bearing quartz (Qz). Data from the Mt Carlton high sulfidation (HS) to intermediate sulfidation (IS) deposit is plotted in green, showing a transition from Ge-rich sulfosalts to Ge-rich sphalerite (Sahlström et al., 2017). An estimated path for the Arre deposit, which shows syn-metamorphic recrystallization of Ge-enriched sphalerite to Ge-oxides and Ge-silicates, is shown in blue (Cugerone et al., 2018).

assuming slightly higher fluid temperatures, e.g. typical of Kipushi-type deposits (250——450 °C). It is therefore probable that an intermediate to high sulfur activity was the main driver for the occurrence of briartite over Ge-enriched sphalerite (Fig. 13). Significant amounts of Ge are also hosted in the silicate-phases phengite and quartz as well as chalcopyrite-1 (Supplementary Table 5). Germanium can be incorporated into chalcopyrite by direct substitution for Fe (Gena et al., 2005; Reiser et al., 2011; Takeno, 1975). With 660 ± 450 ppm and 370 ± 170 ppm, respectively, the Ge concentrations in both phengite and quartz are unusually high (Götze et al., 2021; Monnier et al., 2022). Germanium is most likely hosted as solid solution in the crystal lattice, as both phengite and quartz do not contain any Ge-bearing microinclusions (Supplementary Fig. 4). In silicates Ge substitutes directly for silicon (Goldschmidt, 1926).

Germanium shows differing geochemical behaviour depending on sulfur and oxygen activity (Fig. 13). A change in Ge behaviour during mineralization has been observed at the Mt. Carlton epithermal deposit, where Ge is hosted mainly in sulfosalts and sulfides during a high sulfidation stage, but is then hosted in Ge-rich sphalerite in a later intermediate sulfidation stage (Fig. 13; Sahlström et al., 2017). This effect was caused by decreasing sulfur activity during ore formation (Fig. 13; Sahlström et al., 2017). At the Arre Zn-Pb deposit, Ge hosted in primary sphalerite formed Ge-phases during metamorphic recrystallization of sphalerite under the presence of oxidizing metamorphic fluids, reflecting an increase in oxygen activity (Fig. 13; Cugerone et al., 2018). At South Lakes Glacier, a change in Ge behaviour can be observed as well in stage I. Germanium is first hosted in briartite and chalcopyrite-1, followed by Ge-rich phengite and quartz (Fig. 5). This change from sulfide-hosted to silicate-hosted Ge suggests a decrease in sulfur activity in the ore fluid, and possibly an increase in oxygen activity (Fig. 13). The decrease in sulfur activity likely reflects sulfur removal from the ore fluid by progressive sulfide precipitation.

The occurrence of Ge-enriched, F-bearing phengite at South Lakes Glacier is analogous to phengite from the Ge-bearing Khusib Springs deposit, where F-rich, ore-hosted phengite carries elevated concentrations of Ge (up to 1100 ppm) and Cu (up to ~ 1 %) (Melcher et al., 2006). The Cu concentration in phengite from South Lakes Glacier is however very low (~1 ppm). Nevertheless, this shows that mineralizing fluids carried substantial amounts of Ge. An elevated F concentration in ore fluids, as indicated by F-bearing phengite in both deposits, indicates that F complexes may play a role in the aqueous transport of Ge in these deposits.

### 7.5. Ore fluids and metal sources

Metamorphic rocks can produce metal-rich basement brines (Burisch et al., 2016a; Burisch et al., 2016b; Walter et al., 2018; Walter et al., 2020). The salinity of basement brines is limited (Burisch et al., 2016a), but primary fluid inclusions from the Black Angel mine show high salinities of 30 – 40 % $NaCl_{equiv}$ (Hughes 1982; Konnerup-Madsen, unpublished data) exceeding the salinity range of basement brines. These high salinities may be the result of mixing with evaporite-dissolution brines in the carbonate platform, since anhydrite and scapolite are present in the Mârmorilik Formation as metamorphosed relic evaporites (Rosa et al., 2023). Anhydrite dissolution possibly provided sulfate to the brine (Rosa et al., 2023). In addition to high salinity aqueous fluid inclusions, $CO_2$-$CH_4$ dominated fluid inclusions have been described representing an organic carbon/hydrocarbon-dominated fluid (Hughes 1982; Konnerup-Madsen, unpublished data). Graphite is ubiquitous in the marble, the metapelite and the massive sulfide at South Lakes Glacier and Black Angel, attesting to widespread pre-metamorphic presence of organic carbon. Sulfate reduction and sulfide precipitation were possibly triggered by interaction of a metalliferous, sulfate-bearing brine with hydrocarbon-derived fluids or other organic material (Fig. 12; Scharrer et al., 2022; Scharrer et al., 2021; Walter et al., 2019). Hydrocarbons have been described as critical reducing agent in numerous Zn-Pb deposits (Burisch et al., 2017; Heijlen et al., 2008; Pfaff et al., 2010; Szmihelsky et al., 2020; Walter et al., 2019).

Potassic silicates and quartz have been observed as hydrothermal gangue in numerous carbonate-hosted Zn-Pb deposits, such as MVT, KPT and Irish-type deposits (Chabu and Boulègue, 1992; Leach et al., 2010; Melcher et al., 2006; Riegler and McClenaghan, 2017). Phengite and rare potassic feldspar observed at South Lakes Glacier and Black Angel (this study; Saintilan et al. 2024) likely represent potassic alteration associated with formation of massive sulfides. Phengite can form from hydrothermal fluids with a wide temperature range but requires acidity of the fluid (Cooke et al., 1998; Riegler and McClenaghan, 2017; Velde, 1967). Fluid acidity may have been caused by dissolution of accessory sulfides in basement rocks.

Lead and Zn in the ores of the Black Angel mine were (dominantly) sourced from the local Archean basement (Partin et al., 2021; Saintilan et al., 2024). By extension, metamorphic basement rocks are thus also the most likely source for Cu, Ag and other metals. The source of Ge in ore deposits is however often unclear, but organic matter and basement rocks have been suggested (Luo et al., 2022; Saintilan et al., 2023). It has been demonstrated that unusual pre-enrichment of Zn in basement source rocks is not necessary to form high-grade ore deposits (Walter et al., 2019). A rough estimation after Walter et al. (2019) indicates leaching of a basement gneiss cube with ~ 700 m edge length is sufficient to produce 1 t of briartite, assuming 10 % leaching of a gneiss with average crustal abundance of Ge. Therefore, basement rocks are a reasonable source of Ge. However, due to the organophile behavior of Ge it is also plausible that Ge may have been sourced from organic carbon ubiquitous in the Mârmorilik Formation. Hydrocarbons and organic-rich rocks can contribute significantly to the metal budget of ore fluids and could constitute an alternative Ge source (Melcher et al., 2006; Migdisov et al., 2017; Saintilan et al., 2019; Sośnicka et al., 2023). If Archean basement rocks were the source of Ge, it raises the question of why Ge mineralization is not more prevalent in other ore deposits formed by basement-derived fluids. The relative timing of mineralization seems not to be critical to Ge endowment, as MVT deposits form *syn*-diagenetically and KPT deposits are formed both syn- and post-orogenically (Chetty and Frimmel, 2000; Schneider et al., 2007). Carbonate host rocks and the presence of hydrocarbons/organic matter appear to be the key factors connecting Ge-enriched sulfide deposits. In summary, the mineralization in the Black Angel district likely formed by fluid mixing of an acidic, metalliferous basement brine ascending along normal faults with sulfate-rich evaporite-dissolution brines upon reaching the carbonate platform, and reduction by hydrocarbon-derived fluids (Fig. 12).

The mean Ge grades of 120 ppm and mean Ga grades of 130 ppm from South Lakes Glacier (Supplementary Table 1) are higher than mean Ge whole rock grades published for many Ge-producing and Ge-sulfide bearing deposits like Tsumeb (50 ppm), Khusib Springs (40 ppm) or Kipushi (<60 ppm) (Höll et al., 2007; Ivanhoe Mines, 2015). Germanium occurs almost exclusively in a discrete Ge-mineral and not in sphalerite, where it is typically hosted in. The Black Angel district therefore constitutes a prospective exploration target for high-grade Ge-bearing Zn-Pb deposits.

## 8. Conclusions

The marble-hosted South Lakes Glacier prospect in the Black Angel district is host to substantial amounts of bulk Ge and Ga, both considered critical metals, hosted in high grade Zn-Pb ore. Whereas Ga is mostly hosted in sphalerite, Ge is almost exclusively hosted in briartite, a Ge-sulfide mineral, and not in sphalerite. Two ore stages are observed at South Lakes Glacier: (1) an epigenetic MVT stage with sphalerite, pyrite and galena, that forms the main part of the ore; and (2) a syn-metamorphic stage of renewed fluid flow modifying the primary ore assemblage during retrograde metamorphism. The stage I mineralization was deformed and remobilized during $D_1$ of the Rinkian Orogeny at ca. 510 ± 40 °C, leading to formation of massive sulfide breccias. An overprint by $D_2$ deformation led to small-scale fracturing and a second sulfide remobilization. Briartite, formed during stage I, occurs in two texture types: type I forms up to 3 mm large anhedral to rounded grains with abundant inclusions and type II occurs as small, sphalerite-hosted grains of < 20 μm forming 'briartite disease'. Briartite formed by precipitation from hydrothermal Cu-Ge-bearing fluids as opposed to metamorphic recrystallization of sphalerite, based on grain size, spatial distribution and inclusion in epigenetically formed MVT-stage minerals. Abundant inclusions and flame patterns within briartite likely formed by exsolution during cooling. Ore-hosted phengite and quartz also show unusually high Ge contents and post-date briartite. This marks a shift in Ge behaviour from sulfide-hosted to silicate-hosted, caused by decreasing sulfur activity of the ore fluid. Germanium was either leached from basement rocks by acidic brines along with the other metals, or alternatively, was sourced from organic matter occurring in the Mârmorilik Formation. Sulfide precipitation was likely triggered by fluid mixing of a metalliferous basement brine with evaporite-dissolution brines and hydrocarbon-derived fluids.

## Declaration of competing interest

The authors declare that they have no known competing financial interests or personal relationships that could have appeared to influence the work reported in this paper.

## Acknowledgments

We are grateful to the German Science Foundation (DFG) for financial support (project number 495289842, grants KO 2072/11-1, WA 3116/15-1 and INST 121384/213-1 FUGG). Jochen Kolb thanks the Geological Survey of Denmark and Greenland (GEUS) and the Ministry

of Mineral Resources, Greenland (MMR) for financial support of field expeditions to the study area. We thank Dr. Max Verdugo-Ihl and an anonymous reviewer for thoroughly reviewing the manuscript. Their comments significantly helped to improve the manuscript. Moreover, we are thankful to the editor Huayong Chen for editorial guidance. Dr. Sebastian Staude (University of Tübingen) is thankfully acknowledged for his assistance with EMPA analyses. We thank Prof. Dr. Kirsten Drüppel (KIT) for her help with Raman spectroscopy, Dr. Aratz Beranoaguirre and Dr. Antonin Bilau (KIT) for their guidance with LA-ICP-MS work.

## Appendix A. Supplementary data

Supplementary data to this article can be found online at https://doi.org/10.1016/j.oregeorev.2026.107117.

## Data availability

Data will be made available on request.

## References

Barber, D.J., Heard, H.C., Wenk, H.-R., 1981. Deformation of Dolomite Single Crystals from 20-800 °C. Phys. Chem. Miner. 7, 271–286. https://doi.org/10.1007/BF00311980.

Belissont, R., Boiron, M.-C., Luais, B., Cathelineau, M., 2014. LA-ICP-MS analyses of minor and trace elements and bulk Ge isotopes in zoned Ge-rich sphalerites from the Noailhac – Saint-Salvy deposit (France): Insights into incorporation mechanisms and ore deposition processes. Geochim. Cosmochim. Acta 126, 518–540. https://doi.org/10.1016/j.gca.2013.10.052.

Belissont, R., Muñoz, M., Boiron, M.-C., Luais, B., Mathon, O., 2016. Distribution and oxidation state of Ge, Cu and Fe in sphalerite by μ-XRF and K-edge μ-XANES: insights into Ge incorporation, partitioning and isotopic fractionation. Geochim. Cosmochim. Acta 177, 298–314. https://doi.org/10.1016/j.gca.2016.01.001.

Bernstein, L.R., 1985. Germanium geochemistry and mineralogy. Geochim. Cosmochim. Acta 49 (11), 2409–2422. https://doi.org/10.1016/0016-7037(85)90241-8.

Beyssac, O., et al., 2003. On the characterization of disordered and heterogeneous carbonaceous materials by Raman spectroscopy. Spectrochim. Acta A Mol. Biomol. Spectrosc. 59 (10), 2267–2276. https://doi.org/10.1016/s1386-1425(03)00070-2.

Bogdanov, K., Tsonev, D., Popov, K., 2004. Mineral Assemblages and Genesis of the Cu-Au Epithermal Deposits In the Southern Part of the Panaguyrishte Ore District, Bulgaria. Bull. Geol. Soc. Greece 36, 406–415. https://doi.org/10.12681/bgsg.16726.

Burisch, M., et al., 2017. Methane and the origin of five-element veins: Mineralogy, age, fluid inclusion chemistry and ore forming processes in the Odenwald, SW Germany. Ore Geol. Rev. 81, 42–61. https://doi.org/10.1016/j.oregeorev.2016.10.033.

Burisch, M., Marks, M.A.W., Nowak, M., Markl, G., 2016. The effect of temperature and cataclastic deformation on the composition of upper crustal fluids — an experimental approach. Chem. Geol. 433, 24–35. https://doi.org/10.1016/j.chemgeo.2016.03.031.

Burisch, M., Walter, B.F., Wälle, M., Markl, G., 2016. Tracing fluid migration pathways in the root zone below unconformity-related hydrothermal veins: Insights from trace element systematics of individual fluid inclusions. Chem. Geol. 429, 44–50. https://doi.org/10.1016/j.chemgeo.2016.03.004.

Chabu, M., Boulègue, J., 1992. Barian feldspar and muscovite from the Kipushi Zn-Pb-Cu deposit, Shaba, Zaire. Can. Mineral. 30, 1143–1152.

Chetty, D., Frimmel, H.E., 2000. The role of evaporites in the genesis of base metal sulphide mineralisation in the Northern Platform of the Pan-African Damara Belt, Namibia: geochemical and fluid inclusion evidence from carbonate wall rock alteration. Miner. Deposita 35, 364–376. https://doi.org/10.1007/s001260050247.

Cook, N.J., Halls, C., Boyle, A.P., 1993. Deformation and metamorphism of massive sulphides at Sulitjelma, Norway. Mineral. Mag. 57, 67–81. https://doi.org/10.1180/minmag.1993.057.386.07.

Cooke, D.R., Bull, S., Donovan, S., Rogers, J.R., 1998. K-Metasomatism and Base Metal Depletion in Volcanic Rocks from the McArthur Basin, Northern Territory-Implications for Base Metal Mineralization. Econ. Geol. 93, 1237–1263. https://doi.org/10.2113/gsecongeo.93.8.1237.

Craig, J.R., Vokes, F.M., Solberg, T.N., 1998. Pyrite: physical and chemical textures. Miner. Deposita 34, 82–101. https://doi.org/10.1007/s001260050187.

Cugerone, A., et al., 2018. Relationships between the occurrence of accessory Ge-minerals and sphalerite in Variscan Pb-Zn deposits of the Bossost anticlinorium, French Pyrenean Axial Zone: Chemistry, microstructures and ore-deposit setting. Ore Geol. Rev. 95, 1–19. https://doi.org/10.1016/j.oregeorev.2018.02.016.

Cugerone, A., et al., 2021. Behavior of critical metals in metamorphosed Pb-Zn ore deposits: example from the Pyrenean Axial Zone. Miner. Deposita 56 (4), 685–705. https://doi.org/10.1007/s00126-020-01000-9.

Cugerone, A., et al., 2020. Redistribution of germanium during dynamic recrystallization of sphalerite. Geology 48 (3), 236–241. https://doi.org/10.1130/G46791.1.

De Vos, W., Viaene, W., Moreau, J., 1974. Minéralogie du gisement du Kipushi, Shaba, Zaïre. Centenaire De La Société Géologique De Belgique - Gisments Stratiformes et Provinces Cuprifères 165–183.

Denisová, N., Piercey, S.J., Wälle, M., 2023. Mineralogy and mineral chemistry of the ABM replacement-style volcanogenic massive sulfide deposit, Finlayson Lake district, Yukon, Canada. Mineralium Deposita. doi: 10.1007/s00126-023-01217-4.

Einaudi, M.T., Hedenquist, J.W., Inan, E.E., 2003. Sulfidation State of Fluids in active and Extinct Hydrothermal Systems: Transitions from Porphyry to Epithermal Environments. Society of Economic Geologists Special Publication 10, 285–314.

European Commission, 2020. Critical Raw Materials Resilience: Charting a Path towards greater Security and Sustainability.

Fougerouse, D., Cugerone, A., Reddy, S.M., Luo, K., Motto-Ros, V., 2023. Nanoscale distribution of Ge in Cu-rich sphalerite. Geochim. Cosmochim. Acta 346, 223–230. https://doi.org/10.1016/j.gca.2023.02.011.

Fougerouse, D., et al., 2016. The golden ark: arsenopyrite crystal plasticity and the retention of gold through high strain and metamorphism. Terra Nova 28 (3), 181–187. https://doi.org/10.1111/ter.12206.

Francotte, J., Moreau, J., Ottenburgs, R., Lévy, C., 1965. La briartite, Cu2(Fe,Zn)GeS4, une nouvelle espèce minérale. Bulletin De La Société Française De Minéralogie et De Cristallographie 88 (3), 432–437.

Frenzel, M., Hirsch, T., Gutzmer, J., 2016. Gallium, germanium, indium, and other trace and minor elements in sphalerite as a function of deposit type — a meta-analysis. Ore Geol. Rev. 76, 52–78. https://doi.org/10.1016/j.oregeorev.2015.12.017.

Geier, B.H., Otteman, J., 1970. New Primary Vanadium-, Germanium-, Gallium-, and TinMinerals from the Pb-Zn-Cu-Deposit Tsumeb, South West Africa. Miner. Deposita 5, 29–40. https://doi.org/10.1007/BF00207004.

Gena, K., Chiba, H., Kase, K., 2005. Tin-bearing chalcopyrite and platinum-bearing bismuthinite in the active Tiger chimney, Yonaguni Knoll IV seafloor hydrothermal system, South Okinawa Trough, Japan. Okayama University Earth Science Reports 12 (1), 1–5. https://doi.org/10.18926/ESR/13850.

Gilligan, L.B., Marshall, B., 1987. Textural evidence for remobilization in metamorphic environments. Ore Geol. Rev. 2, 205–229. https://doi.org/10.1016/0169-1368(87)90029-1.

Goldschmidt, V.M., 1926. Über das krystallochemische und geochemische Verhalten des Germaniums. Naturwissenschaften 14, 295–297. https://doi.org/10.1007/BF01503585.

Götze, J., Pan, Y., Müller, A., 2021. Mineralogy and mineral chemistry of quartz: a review. Mineral. Mag. 85 (5), 639–664. https://doi.org/10.1180/mgm.2021.72.

Grocott, J., McCaffrey, K., 2017. Basin evolution and destruction in an Early Proterozoic continental margin: the Rinkian fold–thrust belt of central West Greenland. J. Geol. Soc. London 174 (3), 453–467. https://doi.org/10.1144/jgs2016-109.

Grocott, J., Thrane, K., McCaffrey, K.J.W., Sleath, P.R., Dziggel, A., 2023. Andean-type, bivergent crustal shortening in the Rinkian orogen: New constraints on the tectonic evolution of Laurentia–West Greenland in the Paleoproterozoic. Geosphere 19 (5). https://doi.org/10.1130/GES02614.1.

Guarnieri, P., Baker, N., 2022. Tectonic inversion of listric normal faults in the foreland of the Rinkian Orogen (Maarmorilik, central West Greenland). J. Struct. Geol. 159. https://doi.org/10.1016/j.jsg.2022.104598.

Guarnieri, P., Baker, N., Rosa, D., Sørensen, E.V., 2022. Geological map of Greenland 1: 100 000, Maarmorilik 71 V. 2 Syd. Geological Survey of Denmark and Greenland, Copenhagen. doi: 10.22008/FK2/07OYKX.

Guarnieri, P., et al., 2023. Tectonics of the Paleoproterozoic Rinkian orogen, central West Greenland. Geol. Soc. Am. Bull. https://doi.org/10.1130/B36930.1.

Harris, C.J., 1986. Greenex 1985 Black Angel Surface Drilling Year End Report. Greenex A/S (From GEUS archive, report file no. 20401).

Heijlen, W., Banks, D., Muchez, P., Stensgard, B.M., Yardley, B.W., 2008. The Nature of Mineralizing Fluids of the Kipushi Zn-Cu Deposit, Katanga, Democratic Repubic of Congo: Quantitative Fluid Inclusion Analysis using Laser Ablation ICP-MS and Bulk Crush-Leach Methods. Econ. Geol. 103, 1459–1482. https://doi.org/10.2113/gsecongeo.103.7.1459.

Henderson, G., Pulvertaft, P.C.R., 1987. Geological Map of Greenland, 1:100 000, Mârmorilik 71 V.2 Syd, Nûgâtsiaq 71 V.2 Nord, Pangnertôq 72 V.2 Syd. Descriptive text. Geological Survey of Greenland, Copenhagen.

Henry, D.J., 2005. The Ti-saturation surface for low-to-medium pressure metapelitic biotites: Implications for geothermometry and Ti-substitution mechanisms. Am. Mineral. 90 (2–3), 316–328. https://doi.org/10.2138/am.2005.1498.

Höll, R., Kling, M., Schroll, E., 2007. Metallogenesis of germanium - a review. Ore Geol. Rev. 30 (3–4), 145–180. https://doi.org/10.1016/j.oregeorev.2005.07.034.

Horn, S., Dziggel, A., Kolb, J., Sindern, S., 2019. Textural characteristics and trace element distribution in carbonate-hosted Zn-Pb-Ag ores at the Paleoproterozoic Black Angel deposit, central West Greenland. Miner. Deposita 54 (4), 507–524. https://doi.org/10.1007/s00126-018-0821-5.

Hughes, R.W.B., 1982. A Study of the Mineralisation in the Marmorilik Region, Central Western Greenland. Bachelor Thesis, University of London and Imperial College of Science and Technology London (GEUS Report File no. 20420), 137 pp.

Intiomale, M.M., Oosterbosch, R., 1974. Géologie et Géochimie du Gisement de Kipushi, Zaïre. Centenaire De La Société Géologique De Belgique - Gisments Stratiformes et Provinces Cuprifères 123–164.

Ivanhoe Mines, 2015. Ivanhoe Mines reports additional high-grade zinc, copper, silver and germanium drill results from ongoing exploration program at the Kipushi Mine in the Democratic Republic of Congo, Press Release.

Kamona, A.F., Friedrich, G.H., 2007. Geology, mineralogy and stable isotope geochemistry of the Kabwe carbonate-hosted Pb–Zn deposit, Central Zambia. Ore Geol. Rev. 30 (3–4), 217–243. https://doi.org/10.1016/j.oregeorev.2006.02.003.

Kampunzu, A.B., Cailteux, J.L.H., Kamona, A.F., Intiomale, M.M., Melcher, F., 2009. Sediment-hosted Zn–Pb–Cu deposits in the Central African Copperbelt. Ore Geol. Rev. 35 (3–4), 263–297. https://doi.org/10.1016/j.oregeorev.2009.02.003.
Kelly, A., Knowles, K.M., 2012. Crystallography and Crystal Defects. John Wiley & Sons, Ltd. ISBN: 978-1-119-42017-0.
King, A.R., 1983. Report on Prospecting and Correlation Programme in the Maarmorilik Formation, West Greenland 1982. Greenex A/S (From GEUS archive, report file no. 20386).
Kirkland, C.L., et al., 2017. Apatite and titanite from the Karrat Group, Greenland; implications for charting the thermal evolution of crust from the U-Pb geochronology of common Pb bearing phases. Precambr. Res. 300, 107–120. https://doi.org/10.1016/j.precamres.2017.07.033.
Kretschmar, U., Scott, S.D., 1976. Phase Relations Involving Arsenopyrite in the System Fe-As-S and their Application. Can. Mineral. 14, 364–386.
Leach, D., R.D, T., D.L, F., S.F., D., R.W., S., 2010. A Deposit Model for Mississippi Valley-Type Lead-Zinc Ores: Chapter A in Mineral deposit models for resource assessment., USGS. doi: 10.3133/sir20105070A.
Liu, W., et al., 2023. Germanium speciation in experimental and natural sphalerite: Implications for critical metal enrichment in hydrothermal Zn-Pb ores. Geochim. Cosmochim. Acta 342, 198–214. https://doi.org/10.1016/j.gca.2022.11.031.
Lünsdorf, N.K., Dunkl, I., Schmidt, B.C., Rantitsch, G., von Eynatten, H., 2017. Towards a Higher Comparability of Geothermometric Data Obtained by Raman Spectroscopy of Carbonaceous Material. Part 2: a revised Geothermometer. Geostand. Geoanal. Res. 41 (4), 593–612. https://doi.org/10.1111/ggr.12178.
Lünsdorf, N.K., Lünsdorf, J.O., 2016. Evaluating Raman spectra of carbonaceous matter by automated, iterative curve-fitting. Int. J. Coal Geol. 160–161, 51–62. https://doi.org/10.1016/j.coal.2016.04.008.
Luo, K., et al., 2022. Germanium enrichment in sphalerite with acicular and euhedral textures: an example from the Zhulingou carbonate-hosted Zn(-Ge) deposit, South China. Mineralium Deposita 57 (8), 1343–1365. https://doi.org/10.1007/s00126-022-01112-4.
Marshall, B., Gilligan, L., 1987. An introduction to remobilization: Information from ore-body geometry and experimental considerations. Ore Geol. Rev. 2, 87–131.
Marshall, B., Gilligan, L.B., 1993. Remobilization, syn-tectonic processes and massive sulphide deposits. Ore Geol. Rev. 8, 39–64. https://doi.org/10.1016/0169-1368(87)90025-4.
Melcher, F., 2003. The Otavi Mountain Land In Namibia: Tsumeb, Germanium and Snowball Earth. Mitteilungen Der Österreichischen Mineralogischen Gesellschaft 148, 123–145.
Melcher, F., Oberthür, T., Rammlmair, D., 2006. Geochemical and mineralogical distribution of germanium in the Khusib Springs Cu–Zn–Pb–Ag sulfide deposit, Otavi Mountain Land, Namibia. Ore Geology Reviews 28 (1), 32–56. https://doi.org/10.1016/j.oregeorev.2005.04.006.
Migdisov, A.A., et al., 2017. Hydrocarbons as ore fluids. Geochem. Perspect. Lett. 47–52. https://doi.org/10.7185/geochemlet.1745.
Monnier, L., et al., 2022. Mica trace-element signatures: Highlighting superimposed W-Sn mineralizations and fluid sources. Chem. Geol. 600. https://doi.org/10.1016/j.chemgeo.2022.120866.
Onuk, P., Melcher, F., Mertz-Kraus, R., Gäbler, H.E., Goldmann, S., 2016. Development of a Matrix-Matched Sphalerite Reference Material (MUL-ZnS-1) for Calibration of In Situ Trace Element Measurements by Laser Ablation-Inductively coupled Plasma-Mass Spectrometry. Geostand. Geoanal. Res. 41 (2), 263–272. https://doi.org/10.1111/ggr.12154.
Paar, W.H., Putz, H., 2005. Germanium associated with epithermal mineralization: examples from Bolivia and Argentina. In: Mao J, FP, B. (Eds.), Mineral deposit research: meeting the global challenge, Beijing, pp. 48–51.
Paradis, S., 2015. Indium, germanium and gallium in volcanic- and sediment-hosted base-metal sulphide deposits, Symposium on Strategic and Critical Materials Proceedings.
Partin, C.A., DeWolfe, Y.M., Magee, T., 2021. Origin of sediment-hosted Pb-Zn mineralization in the Paleoproterozoic Mârmorilik and Qaarsukassak formations, Karrat Group, West Greenland. Ore Geology Reviews 134. https://doi.org/10.1016/j.oregeorev.2021.104164.
Partin, C.A., et al., 2024. Geochronology (zircon U-Pb, Hf, O isotopes), provenance analysis, and tectonic setting of the Paleoproterozoic Karrat Group and supracrustal rocks of the Rinkian fold belt, West Greenland. Gondw. Res. 134, 222–244. https://doi.org/10.1016/j.gr.2024.07.011.
Paton, C., Hellstrom, J., Paul, B., Woodhead, J., Hergt;, J., 2011. Iolite: Freeware for the visualisation and processing of mass spectrometric data. J. Anal. At. Spectrom 26 (12). https://doi.org/10.1039/C1JA10172B.
Pedersen, F.D., 1978. Report on Geological Fieldwork 1978. Greenex A/S Utilization and Exploration Concessions, Marmorilik District, West Greenland. Greenex A/S (From GEUS archive, report file no. 20370).
Pedersen, F.D., 1980. Remobilization of the Massive Sulfide Ore of the Black Angel Mine, Central West Greenland. Econ. Geol. 75, 1022–1041. https://doi.org/10.2113/gsecongeo.75.7.1022.
Pedersen, F.D., 1981. Polyphase Deformation of the Massive Sulphide Ore of the Black Angel Mine, Central West Greenland. Miner. Deposita 16, 157–176. https://doi.org/10.1007/BF00206461.
Pfaff, K., Hildebrandt, L.H., Leach, D.L., Jacob, D.E., Markl, G., 2010. Formation of the Wiesloch Mississippi Valley-type Zn-Pb-Ag deposit in the extensional setting of the Upper Rhinegraben, SW Germany. Mineralium Deposita 45 (7), 647–666. https://doi.org/10.1007/s00126-010-0296-5.
Piazolo, S., et al., 2016. Deformation-induced trace element redistribution in zircon revealed using atom probe tomography. Nat. Commun. 7, 10490. https://doi.org/10.1038/ncomms10490.
Reiser, F.K.M., et al., 2011. Mineralogy and geochemistry of tin- and germanium-bearing copper ore, Barrigão re-mobilized vein deposit, Iberian Pyrite Belt, Portugal. International Geology Review 53 (10), 1212–1238. https://doi.org/10.1080/00206811003683168.
Riegler, T., McClenaghan, S.H., 2017. Authigenic potassic silicates in the Rathdowney Trend, southwest Ireland: New perspectives for ore genesis from petrography of gangue phases in Irish-type carbonate-hosted Zn-Pb deposits. Ore Geol. Rev. 88, 140–155. https://doi.org/10.1016/j.oregeorev.2017.04.017.
Rosa, D., Leach, D., Guarnieri, P., Bekker, A., 2023. The Black Angel deposit, Greenland: a Paleoproterozoic evaporite-related Mississippi Valley-type Zn–Pb deposit. Miner. Deposita 58, 51–73. https://doi.org/10.1007/s00126-022-01125-z.
Sahlström, F., Arribas, A., Dirks, P., Corral, I., Chang, Z., 2017. Mineralogical distribution of Germanium, Gallium and Indium at the Mt Carlton High-Sulfidation Epithermal Deposit, NE Australia, and Comparison with Similar deposits Worldwide. Minerals 7, 213–241. https://doi.org/10.3390/min7110213.
Saintilan, N.J., et al., 2024. Paleoproterozoic Mississippi Valley-type mineralization at Black Angel, Greenland: evidence from sulfide δ66Zn and rhenium-osmium geochronology. Miner. Deposita. https://doi.org/10.1007/s00126-024-01332-w.
Saintilan, N.J., Archer, C., Szilas, K., Rosa, D., 2023. Co-evolution of pyrite d66Zn and sphalerite-pyrite-galena modal proportions in the ca. 1,828 Ma Mississippi Valley type Zn-Pb Black Angel deposit, Greenland: insights into the chemical potential of sedimentary carbonates for Zn mineralization, 17th SGA Biennial Meeting, Zürich.
Saintilan, N.J., et al., 2019. Petroleum as source and carrier of metals in epigenetic sediment-hosted mineralization. Sci. Rep. 9 (1), 8283. https://doi.org/10.1038/s41598-019-44770-7.
Scharrer, M., Epp, T., Walter, B.F., Pfaff, D.K., Venneman, T., Markl, G., 2022. The formation of (Ni-Co-Sb)-Ag-As ore shoots in hydrothermal galena-sphalerite-fuorite veins. Miner. Deposita 57, 853–885. https://doi.org/10.1007/s00126-021-01059-y.
Scharrer, M., Reich, R., Fusswinkel, T., Walter, B.F., Markl, G., 2021. Basement aquifer evolution and the formation of unconformity-related hydrothermal vein deposits: LA-ICP-MS analyses of single fluid inclusions in fluorite from SW Germany. Chem. Geol. 575. https://doi.org/10.1016/j.chemgeo.2021.120260.
Schneider, J., Melcher, F., Brauns, M., 2007. Concordant ages for the giant Kipushi base metal deposit (DR Congo) from direct Rb–Sr and Re–Os dating of sulfides. Miner. Deposita 42 (7), 791–797. https://doi.org/10.1007/s00126-007-0158-y.
Shanks, W.C.P.I., Kimball, B.E., Tolcin, A.C., Guberman, D.E., 2017. Germanium and Indium. In: Klaus J. Schulz, J.H.D., Jr., Robert R. Seal II, and Dwight C. Bradley (Ed.), Critical Mineral Resources of the United States—Economic and Environmental Geology and Prospects for Future Supply. Professional Paper 1802–I. doi:10.3133/pp1802I.
Sharp, Z.D., Essene, E.J., Kelly, W.C., 1985. A Re-Examination of the Arsenopyrite Geothermometer: pressure Considerations and applications to Natural Assemblages. Can. Mineral. 23, 517–534.
Sidgren, A.-S., Page, L., Garde, A.A., 2006. New hornblende and muscovite 40Ar/39Ar cooling ages in the central Rinkian fold belt, West Greenland. Geological Survey of Denmark and Greenland Bulletin 11, 115–123. https://doi.org/10.34194/geusb.v11.4920.
Skinner, B.J., Johnson, C.A., 1987. Evidence for movement of ore materials during high grade metamorphism. Ore Geol. Rev. 2, 191–204. https://doi.org/10.1016/0169-1368(87)90028-X.
Sośnicka, M., et al., 2023. Metal budget and origin of aqueous brines depositing deep-seated Zn-Pb mineralization linked to hydrocarbon reservoirs, North German Basin. Mineralium Deposita 58 (6), 1143–1170. https://doi.org/10.1007/s00126-023-01173-z.
Stipp, M., Stünitz, H., Heilbronner, R., Schmid, S.M., 2002. The eastern Tonale fault zone: a 'natural laboratory' for crystal plastic deformation of quartz over a temperature range from 250 to 700°C. J. Struct. Geol. 24 (12), 1861–1884. https://doi.org/10.1016/S0191-8141(02)00035-4.
Szmihelsky, M., et al., 2020. Mixing of brine with oil triggered sphalerite deposition at Pine Point, Northwest Territories. Canada. Geology 49 (5), 488–492. https://doi.org/10.1130/G48259.1.
Takeno, S., 1975. The pseudobinary system briartite-chalcopyrite. Neues Jahrbuch Für Mineralogie Monatshefte 7, 294–299.
Thomassen, B., 2003. The Black Angel lead-zinc mine at Maarmorilik in West Greenland. Geology and Ore 2. https://doi.org/10.22008/gpub/38348.
Thrane, K., 2021. The oldest part of the Rae craton identified in western Greenland. Precambr. Res. 357. https://doi.org/10.1016/j.precamres.2021.106139.
Tiu, G., Jansson, N., Wanhainen, C., Ghorbani, Y., Lilja, L., 2021. Ore mineralogy and trace element (re)distribution at the metamorphosed Lappberget Zn-Pb-Ag-(Cu-Au) deposit, Garpenberg. Sweden. Ore Geology Reviews 135. https://doi.org/10.1016/j.oregeorev.2021.104223.
Tomkins, A.G., 2007. Three mechanisms of ore re-mobilisation during amphibolite facies metamorphism at the Montauban Zn–Pb–Au–Ag deposit. Miner. Deposita 42 (6), 627–637. https://doi.org/10.1007/s00126-007-0131-9.
Torró, L., et al., 2023. Germanium- and gallium-rich sphalerite in Mississippi Valley–type deposits: the San Vicente district and the Shalipayco deposit, Peru. Mineralium Deposita 58 (5), 853–880. https://doi.org/10.1007/s00126-023-01160-4.
U.S. Geological Survey, 2024. Mineral commodity summaries 2024. U.S. Geological Survey, pp. 212 p. doi:10.3133/mcs2024.
van der Stijl, F.W., 1990. Status of pillar reserves, August 1st 1990. Black Angel Mine and Nunngarut, Greenex A/S Internal Report.
Velde, B., 1967. Si+4 Content of Natural Phengites. Contrib. Miner. Petrol. 14, 250–258. https://doi.org/10.1007/BF00376643.
Vikentyev, I.V., Belogub, E.V., Novoselov, K.A., Moloshag, V.P., 2016. Metamorphism of volcanogenic massive sulphide deposits in the Urals. Ore Geology. Ore Geology Reviews 85, 30–63. https://doi.org/10.1016/j.oregeorev.2016.10.032.

Vokes, F.M., 1969. A review of the metamorphism of sulphide deposits. Earth Sci. Rev. 5 (2), 99–143. https://doi.org/10.1016/0012-8252(69)90080-4.
Vukmanovic, Z., et al., 2014. Relationship between microstructures and grain-scale trace element distribution in komatiite-hosted magmatic sulphide ores. Lithos 184–187, 42–61. https://doi.org/10.1016/j.lithos.2013.10.037.
Wagner, T., Monecke, T., 2005. Germanium-Bearing Colusite from the Waterloo Volcanic-Rock-Hosted Massive Sulfide Deposit, Australia: Crystal Chemistry and Formation of Colusite-Group Minerals. Can. Mineral. 43, 655–669. https://doi.org/10.2113/gscanmin.43.2.655.
Walter, B.F., et al., 2018. Multi-reservoir fluid mixing processes in rift-related hydrothermal veins, Schwarzwald, SW-Germany. J. Geochem. Explor. 186, 158–186. https://doi.org/10.1016/j.gexplo.2017.12.004.
Walter, B.F., et al., 2020. Formation of hydrothermal fluorite-hematite veins by mixing of continental basement brine and redbed-derived fluid: Schwarzwald mining district, SW-Germany. Journal of Geochemical Exploration 212. https://doi.org/10.1016/j.gexplo.2020.106512.
Walter, B.F., et al., 2019. Chemical evolution of ore-forming brines – Basement leaching, metal provenance, and the redox link between barren and ore-bearing hydrothermal veins. a case study from the Schwarzwald mining district in SW-Germany. Chem. Geol. 506, 126–148. https://doi.org/10.1016/j.chemgeo.2018.12.038.
Wilson, S.A., Ridley, W.I., Koenig, A.E., 2002. Development of sulfide calibration standards for the laser ablation inductively-coupled plasma mass spectrometry technique. J. Anal. At. Spectrom 17 (4), 406–409. https://doi.org/10.1039/b108787h.
Wise, S.A., Wattens, R.L., 2012a. Certificate of Analysis: Standard Reference Material 612. National Institute of Standards and Technology: Gaithersburg, MD, USA.
Wise, S.A., Wattens, R.L., 2012b. Certificate of Analysis: Standard Reference Material 614. National Institute of Standards and Technology: Gaithersburg, MD, USA.
Wu, C.-M., Chen, H.-X., 2015. Revised Ti-in-biotite geothermometer for ilmenite- or rutile-bearing crustal metapelites. Science Bulletin 60 (1), 116–121. https://doi.org/10.1007/s11434-014-0674-y.
Zheng, Y., et al., 2012. Sulfide Remobilisation from Sulfide Ore at High Temperatures and Differential Stresses: An Experimental Approach. Resour. Geol. 62 (2), 174–186. https://doi.org/10.1111/j.1751-3928.2012.00187.x.